2

ARTIFICIAL TRANSMISSION LINES BASED ON PERIODIC STRUCTURES

2.1 INTRODUCTION AND SCOPE

In the framework of RF/microwave engineering, one-dimensional periodic structures are transmission lines and waveguides periodically loaded with identical elements (lumped, semilumped, inclusions, defects, etc.), or with a periodic perturbation in their cross-sectional geometry (nonuniform transmission lines and waveguides).[1] The main relevant properties of one-dimensional periodic structures, which will be reviewed in this chapter, can be useful for the implementation of artificial transmission lines with various functionalities and applications based on them. Specifically, periodic transmission lines exhibit stop/pass bands, and support the propagation of waves with phase velocities lower (slow waves) or higher (fast waves) than the speed of light. Thus, transmission lines based on periodic structures can be applied to the implementation of filters, reflectors, electromagnetic bandgaps (EBGs),[2] slow wave structures

[1] Two-dimensional and three-dimensional periodic structures can also be of interest at RF/microwave (and even at optical) frequencies, in applications such as frequency-selective surfaces, antenna substrates and superstrates (to improve antenna performance), isolators, and so on, but these structures are out of the scope of this book, which is focused on artificial transmission lines.

[2] In analogy with semiconductor crystals (which exhibit forbidden energy bands, or gaps), periodic structures in the optical domain are usually identified as photonic crystals (PCs), or photonic bandgaps (PBGs). This explains the term "electromagnetic bandgap" (EBG) used to designate such structures at RF/microwave frequencies.

Artificial Transmission Lines for RF and Microwave Applications, First Edition. Ferran Martín.

(of interest for device miniaturization), and leaky wave antennas (LWAs), among others.

The purpose of this chapter is to briefly present the Floquet (or Bloch mode) analysis of one-dimensional periodic structures (which will bring us to the concept of space harmonics), and the transfer matrix method, applied to the unit cell, for obtaining the modal solutions (or dispersion curves) of the fundamental space harmonic. This will be important to predict the frequency response of the considered lines based on periodic structures. Moreover, an alternative and complementary analysis for periodic transmission lines with nonuniform cross section, (e.g., microstrip lines with defected ground planes or strip width modulation), based on the coupled mode theory, is also included in this chapter. By means of justified approximations, it will be shown that this analysis provides valuable information (through analytical expressions) relative to the main relevant parameters of these lines (S-parameters, maximum reflectivity and bandwidth of the stop bands, etc.). The periodic transmission lines that will be considered and studied in this chapter through the earlier-cited approaches (the transfer matrix method and the coupled mode analysis) include EBG-based transmission lines (either with defected ground planes or strip width modulation), and transmission lines loaded with reactive elements. The main applications of these lines will also be reviewed in the chapter.

2.2 FLOQUET ANALYSIS OF PERIODIC STRUCTURES[3]

Let us consider a one-dimensional infinite periodic structure (transmission line or waveguide) with period l, and the propagation axis denoted as z. If the time dependence is chosen as $e^{j\omega t}$, and if the cross-sectional dependence is suppressed, the Floquet's theorem states that the fields propagating along the line can be expressed as Bloch waves according to [1–5]:

$$\Psi(z) = e^{-\gamma z} \cdot P(z) \tag{2.1}$$

where γ is the propagation constant, and $P(z)$ is a periodic function with period l:

$$P(z+l) = P(z) \tag{2.2}$$

Thus, the field behavior can be expressed in terms of a fundamental traveling wave, with propagation constant γ, and a standing wave $P(z)$, which repeats in each unit cell

[3] This section is mainly based on a short course given by Arthur A. Oliner, who recently passed away, and who was a pioneer in the topic of periodic structures and leaky waves. His contributions on this topic are so well-written and comprehensible that can be effortlessly understood. Let us consider this section, extracted from this short course (published in Ref. [2]), as a tribute to him.

and represents the local variations due to the periodicity. From (2.1), it follows that the fields at positions separated by one period are related by:

$$\Psi(z+l) = e^{-\gamma(z+l)} \cdot P(z+l) = e^{-\gamma l} \cdot \Psi(z) \tag{2.3}$$

or, in other words, the fields of a Bloch wave repeat at each unit cell terminal, having a propagation factor $e^{-\gamma l}$.

Since $P(z)$ is a periodic function, it can be expanded in a Fourier series as

$$P(z) = \sum_{n=-\infty}^{n=+\infty} P_n e^{-j\frac{2\pi n}{l}z} \tag{2.4}$$

By inserting (2.4) into (2.1), the fields can be expressed as a superposition of traveling waves of the form

$$\Psi(z) = \sum_{n=-\infty}^{n=+\infty} P_n e^{-j\left(\beta+\frac{2\pi n}{l}\right)z} \cdot e^{-\alpha z} \tag{2.5}$$

where the propagation constant has been decomposed into the phase and attenuation constants, $\gamma = \alpha + j\beta$. The components of (2.5) are called space harmonics, in analogy to the harmonic decomposition of a periodic signal in time domain [2, 4]. The phase constants of the space harmonics are thus given by:

$$\beta_n = \beta + \frac{2\pi n}{l}, \; n = 0, \pm 1, \pm 2, \ldots \tag{2.6}$$

and the phase of the fundamental harmonic ($n = 0$) is simply β. It is important to mention that the space harmonics do not exist independently. Rather than being modal solutions by themselves, they represent individual contributions to the whole field.

Since the phase constants of the space harmonics differ by a constant, it follows that the group velocity is the same for all harmonics, that is,

$$v_{\text{gn}} = \frac{d\omega}{d\beta} \tag{2.7}$$

whereas the phase velocities are given by

$$v_{\text{pn}} = \frac{\omega}{\beta + 2\pi n/l} \tag{2.8}$$

From the space harmonics representation of the periodic structure, it is possible to infer the pass/stop band characteristics inherent to periodicity. The reason is mode interference (or coupling) between modes with similar phase velocities but opposite

group velocities (this aspect will be studied in Section 2.4 in detail). This results in stop bands (or gaps) in the frequency response. To gain insight on this effect, let us consider that a transmission line is slightly (periodically) perturbed so that the phase constant β of the fundamental harmonic can be approximated by a straight line (see expression 1.6). This means that the $\beta - \omega$ diagrams (or dispersion curves) of the set of space harmonics, obtained by displacing the dispersion diagram of the fundamental harmonic a quantity $2\pi n/l$, are also straight lines, as depicted in Figure 2.1. This diagram points out that there are points where the straight lines cross, giving rise to mode coupling and hence stop bands, as Figure 2.2 illustrates. Thus, Figure 2.2 depicts the actual dispersion curves of the slightly perturbed transmission line. The gap bandwidths and the specific frequency dependence of the phase constants

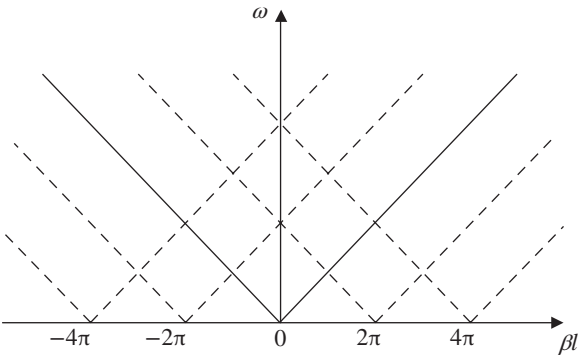

FIGURE 2.1 β-ω diagram of the fundamental harmonic (solid line) and high-order space harmonics (dashed lines) for a transmission line with an infinitesimal periodic perturbation.

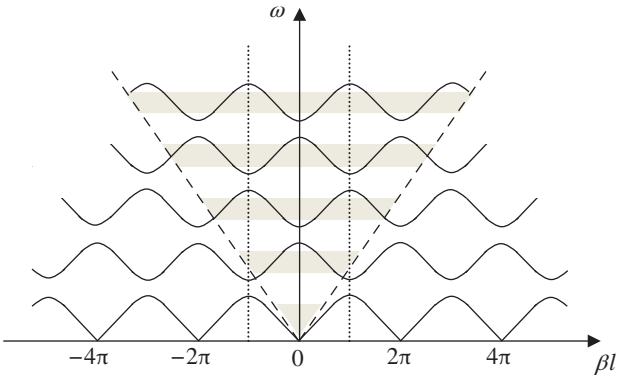

FIGURE 2.2 Dispersion diagram of a one-dimensional periodic structure with space harmonics. The limits of the first Brillouin zone are indicated by vertical dotted lines. The region where leaky wave radiation is possible is delimited by the dashed lines with slopes $-c/l$ and $+c/l$ (and indicated by the gray-white alternating strips).

(identical for all the space harmonics) are related to the nature and magnitude of the perturbation or loading element. Nevertheless, in view of Figure 2.2, the band gaps appear at frequencies satisfying $\beta l = \pi$ (or $l = \lambda/2$), that is,

$$f = \frac{v_p}{2l} \tag{2.9}$$

and its harmonics, v_p being the phase velocity of the unperturbed line. Expression (2.9) is known as the Bragg condition, and states that the first stop band caused by the effects of periodicity[4] appears at the frequency satisfying that the period is half the wavelength of the unperturbed line, λ. The presence of additional band gaps depends on the harmonic content of the Fourier expansion (2.4), which in turn depends on the specificities of the loading elements or perturbation (this aspect will also be considered in Section 2.4).

It is remarkable that the part of the $\beta - \omega$ diagram of Figure 2.2 comprised between $-\pi < \beta l < \pi$ is repetitive every $\beta l = 2\pi$ along the abscissa axis. Usually, this region is referred to as the first Brillouin zone, and the curves within this region give full information of the dispersion characteristics of the periodic structure [1, 5]. It is also important to mention that if we consider either an infinitely long or terminated (with a matched load) periodic transmission line (so that reflections are avoided) fed by a source at one end, the waves excited by the source must carry their energy (and hence the group velocity) in the direction against the source (i.e., toward the load if it is present). Thus, in such situation, only the portions of the curves of Figure 2.2 with positive slope (or group velocity) are of interest.[5] Regardless of the propagation direction, there are regions of the dispersion curves where $\beta(\omega) \cdot d\beta(\omega)/d\omega < 0$. In these regions, the phase and group velocities are of opposite sign, and the corresponding waves are called backward waves.[6]

Another relevant aspect of one-dimensional periodic structures is the fact that these structures may radiate if they are open. The reason is that there are portions of the dispersion curves where the phase velocity is higher than the speed of light in vacuum, c, (fast wave regions, see Fig. 2.2). These radiating harmonics are leaky waves, and exhibit properties similar to leaky waves in uniform structures. A detailed analysis of leaky wave radiation in periodic structures is out of the scope of this book (see [6–9] for further details).[7] Therefore, we will simply present a brief and straightforward

[4] Stop bands not related to periodicity may appear at lower frequencies, for instance, by periodically loading a transmission line with resonators coupled to it. In this case, the first stop band is centered at the resonance frequency of the resonant element.

[5] It is assumed that the energy travels toward the positive z-direction.

[6] The concept of backward wave will be considered in detail in Chapter 3. Nevertheless, it is important to distinguish them from backward travelling waves. In backward waves, the energy propagates in the opposite direction to the phase of the waves, and it is therefore an unconventional type of propagation. Thus, for energy transmission in the positive z-direction, the phase of the waves propagates in the negative/positive z-direction for backward/forward waves. Backward/forward travelling waves are simply forward waves propagating in the negative/positive z-direction.

[7] Nevertheless, we dedicate a subsection in Chapter 4 devoted to LWAs based on metamaterial transmission lines.

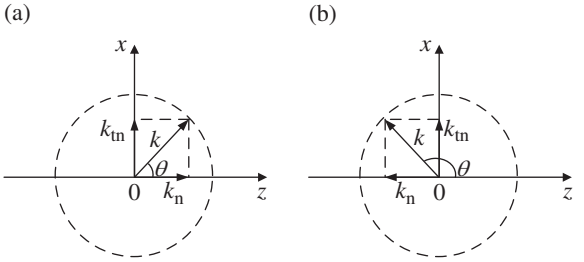

FIGURE 2.3 Diagrams illustrating the generation of a forward (a) and backward (b) leaky wave in a periodic structure.

analysis to understand the phenomenon. Let us consider that the fields in the open periodic structure vary in both the longitudinal and transverse directions. The free-space wavenumber k is related to the parameters of each space harmonic as [2][8]:

$$k^2 = k_{\mathrm{n}}^2 + k_{\mathrm{tn}}^2 = \left(\beta + \frac{2\pi n}{l} - j\alpha\right)^2 + k_{\mathrm{tn}}^2 \tag{2.10}$$

where it has been assumed that $k_{\mathrm{n}} = \beta_{\mathrm{n}} - j\alpha$ (component in the longitudinal direction) and $k_{\mathrm{tn}} = \beta_{\mathrm{tn}} - j\alpha_{\mathrm{tn}}$ (component in the transverse direction). To graphically illustrate the generation of leaky waves by the fast wave space harmonics, let us assume that the longitudinal attenuation constant α is negligible (i.e., $k_{\mathrm{n}} = \beta_{\mathrm{n}}$). In that case, if $k_n{}^2 > k^2$ (slow wave regions), k_{tn} is imaginary, and the mode does not leak. Conversely, if $k_n{}^2 < k^2$ (fast waves), k_{tn} is real and the mode radiates. This situation is illustrated in Figure 2.3, where it can be seen that for $0 < k_n < |k|$ and $-|k| < k_n < 0$, the radiation is forward and backward, respectively. For the specific frequencies where $k_n = 0$, $k_n = |k|$ and $k_n = -|k|$, leaky wave radiation is designated as broadside, endfire and backfire, respectively. Indeed, the direction of the radiated beam can be easily inferred from:

$$\cos\theta = \frac{k_n}{|k|} \tag{2.11}$$

which results from direct inspection to Figure 2.3.

Let us now take into account the attenuation constants in (2.10). Through separation of the real and imaginary parts, we obtain:

$$k^2 = k_n^2 + k_{tn}^2 = \left(\beta_n^2 - \alpha^2 + \beta_{tn}^2 - \alpha_{tn}^2\right) - 2j(\alpha\beta_n + \alpha_{tn}\beta_{tn}) \tag{2.12}$$

[8] The free-space wavenumber is denoted as k, rather than k_0 (as usual), to avoid confusion with the fundamental space harmonic. However, in Section 2.4, we recover the usual designation (see expression 2.45) since in that section k is used as a parameter related to the weighting factors of the coupling coefficient (to be defined later), according to expression (2.66).

Since the imaginary part of the free-space wavenumber k is zero, it follows that

$$\alpha_{tn} = -\alpha \frac{\beta_n}{\beta_{tn}} \tag{2.13}$$

Expression (2.13) is interesting because it points out a significant difference between the forward and backward leaky waves. Namely, since the longitudinal attenuation constant α and transverse phase constant β_{tn} are both positive, the transverse attenuation constant α_{tn} is of opposite sign to the longitudinal phase constant of the space harmonic β_n. Thus, if $\beta_n < 0$, α_{tn} is positive, meaning that the radiated fields decay in the transverse direction. Conversely, if $\beta_n > 0$, α_{tn} is negative, and the fields increase in the transverse direction. In this latter case (forward wave radiation), since this wave type would diverge at infinity in the transverse plane if it were defined everywhere, it cannot be spectral, that is, a proper mode. Therefore forward leaky waves are said to be non-spectral, contrary to backward leaky waves, which are called spectral [2]. By introducing (2.13) into (2.12), the relation between k, β_n and β_{tn} is found to be:

$$\beta_n^2 = \frac{k^2 - \beta_{tn}^2 + \alpha^2}{1 - \dfrac{\alpha^2}{\beta_{tn}^2}} \tag{2.14}$$

Notice that although forward (nonspectral) leaky waves are mathematically improper,[9] they have physical meaning and are useful for the implementation of radiating elements (LWAs). In practice, the leaky wave is defined only within a wedge-shaped region determined by the position of the source, where the leaky wave decays at all angles from the source. This solves the above inconsistency between the mathematical solution and the "physical" leaky waves, never exhibiting progressively increasing fields in the transverse direction.

2.3 THE TRANSFER MATRIX METHOD

Although the space harmonics are fundamental to explain several properties of periodic structures (the weight of each harmonic depends on the nature and magnitude of the perturbation), usually the fundamental space harmonic is dominant, and it suffices for the description of many structures (especially in the pass band regions, far enough from the band gap edges). In order to obtain the modal solutions (or dispersion characteristics) of the fundamental space harmonic (or equivalently of the Bloch wave), the transfer matrix method is very useful in situations where the fields at two positions separated by a period (related by Eq. 2.3) can be expressed as mutually dependent through a certain transfer function (or matrix), characteristic of the unit cell structure.

[9] The increasing field in the transverse direction violates the boundary condition at infinity since the mathematical description of leaky waves holds throughout all space.

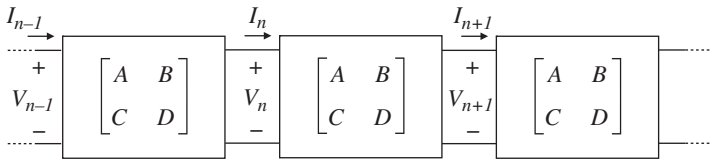

FIGURE 2.4 Periodic structure with unit cell described by the transfer *ABCD* matrix.

2.3.1 Dispersion Relation

Let us consider the periodic structure depicted in Figure 2.4, where the unit cells are represented by boxes, and let us consider that the voltages and currents at the reference planes between adjacent unit cells are well (uniquely) defined[10] and measurable quantities. The voltages and currents on either side of the *n*th unit cell are related by the *ABCD* matrix (see Appendix C) according to

$$\begin{pmatrix} V_n \\ I_n \end{pmatrix} = \begin{pmatrix} A & B \\ C & D \end{pmatrix} \begin{pmatrix} V_{n+1} \\ I_{n+1} \end{pmatrix} \tag{2.15}$$

On the other hand, according to the Floquet's theorem, the voltages and currents at the n and $n+1$ planes only differ by the propagation factor, that is

$$V_{n+1} = e^{-\gamma l} \cdot V_n \tag{2.16a}$$

$$I_{n+1} = e^{-\gamma l} \cdot I_n \tag{2.16b}$$

From (2.15) and (2.16), it follows that

$$\begin{pmatrix} V_n \\ I_n \end{pmatrix} = \begin{pmatrix} A & B \\ C & D \end{pmatrix} \begin{pmatrix} V_{n+1} \\ I_{n+1} \end{pmatrix} = \begin{pmatrix} e^{\gamma l} \cdot V_{n+1} \\ e^{\gamma l} \cdot I_{n+1} \end{pmatrix} \tag{2.17}$$

[10] Strictly speaking, this uniqueness of voltages and currents is only possible for TEM modes, but it can also be made extensive to quasi-TEM modes. For non-TEM modes, the voltage and the current are not properly (uniquely) defined. However, it is possible to define an equivalent voltage and current that make these variables (and even their ratio, the impedance) useful quantities. To this end, the following considerations are applied [10]: (i) voltage and current are only defined for a particular mode, and are defined so that the voltage and current are proportional to the transverse electric and magnetic fields, respectively; (ii) the equivalent voltages and currents should be defined so that their product gives the power flow of the mode; and (iii) the voltage to current ratio for a single travelling wave should be equal to the characteristic impedance of the mode. Nevertheless, unless otherwise specified, the periodic structures considered throughout this book can be described, to a first-order approximation, by considering only the TEM or quasi-TEM modes. Therefore, expression (2.15) involves well-defined variables in our case.

or

$$\begin{pmatrix} A-e^{\gamma l} & B \\ C & D-e^{\gamma l} \end{pmatrix} \begin{pmatrix} V_{n+1} \\ I_{n+1} \end{pmatrix} = 0 \tag{2.18}$$

Notice that, according to (2.17) and (2.18), the voltages and currents propagating in the line are the eigenvectors, whereas the propagation factor is given by the eigenvalues, or eigenmodes, of the system. For a nontrivial solution, the determinant of the matrix in (2.18) must be zero, namely

$$AD + e^{2\gamma l} - (A+D)e^{\gamma l} - BC = 0 \tag{2.19}$$

Since for a reciprocal system $AD - BC = 1$ (see Appendix C), (2.19) can be expressed as follows[11]:

$$e^{\gamma l} + e^{-\gamma l} = A + D \tag{2.20}$$

and the dispersion relation can be finally written as

$$\cosh(\gamma l) = \frac{A+D}{2} \tag{2.21}$$

In a lossless and reciprocal periodic structure, the right-hand side of (2.21) is purely real. This means that the propagation constant is either purely real ($\gamma = \alpha$, $\beta = 0$) or purely imaginary ($\gamma = j\beta$, $\alpha = 0$).[12] In the first case, the Bloch wave is attenuated along the line, and the corresponding regions define the stop bands of the structure. If $\gamma = j\beta$ and $\alpha = 0$, $\cosh(\gamma l) = \cos(\beta l)$, and (2.21) rewrites as follows:

$$\cos(\beta l) = \frac{A+D}{2} \tag{2.22}$$

Expression (2.22) is thus valid in the propagation regions, where the modulus of the right-hand side is smaller than 1. If the unit cell of the periodic structure is symmetric with respect to the plane equidistant from the input and output ports, $A = D$ and (2.22) can be simplified to

$$\cos(\beta l) = A \tag{2.23}$$

[11] Reciprocity is assumed throughout this chapter.

[12] As it will be shown in Chapter 3, under some circumstances, lossless periodic structures may support modes that appear as conjugate pairs, that is, modes of the form $\gamma = \alpha \pm j\beta$. Such modes are called complex modes.

2.3.2 Bloch Impedance

Another important parameter is the relationship between the voltage and current at any position (plane) of the periodic structure. Such parameter can be inferred from (2.18), namely,

$$\left(A - e^{\gamma l}\right) V_{n+1} + B I_{n+1} = 0 \tag{2.24}$$

and it follows that

$$\frac{V_{n+1}}{I_{n+1}} = -\frac{B}{A - e^{\gamma l}}, \ \forall n \tag{2.25}$$

Expression (2.25) does not depend on the plane where such voltage to current relation is calculated. It resembles the characteristic impedance of a transmission line, defined as the relation between voltage and current for a single propagating wave at any position in the line. However, since the propagating waves in the periodic structure are Bloch waves, it is more convenient to identify the impedance given by (2.25) as the Bloch impedance, Z_B. Isolating $e^{\gamma l}$ from (2.20) and introducing it into (2.25), it follows that the Bloch impedance has two solutions:

$$Z_B^{\pm} = -\frac{2B}{A - D \mp \sqrt{(A+D)^2 - 4}} \tag{2.26}$$

one corresponding to forward traveling waves and the other to backward traveling waves. In general, the two solutions of (2.26) are complex. In the propagation regions, $(A + D)^2 < 4$, and the resulting solutions have the same magnitude, identical imaginary part and real parts of opposite sign. In the forbidden (band gap) regions, the two solutions are purely imaginary[13] and exhibit different magnitude, unless the unit cell is symmetric. In this case, $A = D$ and (2.26) is simplified to

$$Z_B^{\pm} = \pm \frac{B}{\sqrt{A^2 - 1}} \tag{2.27}$$

For a lossless and symmetric structure, the two solutions of the Bloch impedance in the allowed regions are real and have opposite signs. Such different signs are indicative of propagation in the forward or backward direction (the negative sign for backward traveling waves is related to the definition of the currents in Fig. 2.4).

Let us discuss the meaning of the complex Bloch impedance that results in the allowed bands of lossless periodic structures with asymmetric unit cells. According

[13] In the forbidden regions, $(A + D)^2 > 4$, hence the denominator in (2.26) is a real number. Since for a lossless structure B is purely imaginary, it follows that the Bloch impedance is purely imaginary in those regions.

to expression (1.8), in a lossless transmission line, the characteristic impedance is purely real. However, the Bloch impedance in lossless periodic structures is complex, if the unit cell is asymmetric. This complex impedance cannot be related to attenuation losses if the periodic line is lossless. The origin of the complex Bloch impedance in lossless periodic structures with asymmetric unit cells is intimately related to the termination of the line. If the unit cell is asymmetric, a finite periodic structure consisting of a certain number of cascaded unit cells is also asymmetric. Therefore, the input impedance of such an asymmetric structure terminated by certain load impedance depends on the locations (left or right) of the source and the load. In particular, if the structure is terminated with the Bloch impedance, the impedance seen from the input port is also the Bloch impedance. However, since the input impedance depends on the position of the source (input port), it follows that the Bloch impedance must be different for forward and backward traveling waves in asymmetric periodic transmission lines. Nevertheless, for an infinite periodic structure, where the effects of terminations vanish, propagation in the forward or backward directions must be undistinguishable. Indeed, if the structure is infinite, it can be described by a cascade of symmetric unit cells, by simply shifting the reference planes, as described in Figure 2.5.[14] Since the Bloch impedance for this symmetric unit-cell-based structure in the propagation regions is real, we can conclude that the complex Bloch impedance in the asymmetric structure is caused by a phase shift in only one of the variables (voltage or current), as compared to the symmetric case (where voltage and current are in phase), as consequence of a displacement of the reference planes (this situation is also illustrated in Fig. 2.5). From this analysis, we can also conclude that for both forward and backward traveling waves propagating in the periodic structure with asymmetric unit cells, the real part of the Bloch impedance must be identical, whereas the imaginary parts must have identical magnitude and different sign (for the validity of this statement, we have assumed that the backward traveling waves exhibit positive current in the backward direction).

To gain insight on the effects of asymmetry, let us consider a periodic structure that can be described by the network of Figure 2.5, where the dashed lines are the reference planes for the symmetric unit cell described by a T-circuit model, whereas the dotted lines are the reference planes of the asymmetric unit cell described by an L-circuit.[15] The elements of the *ABCD* matrix for the unit cells considered in Figure 2.5 can be easily inferred [10]. In particular, for the symmetric unit cell:

$$A = D = 1 + \frac{Z_s}{2Z_p} \tag{2.28a}$$

[14] This statement is based on the fact that any two-port network can be described by means of an equivalent π- or T-circuit. Despite the asymmetry of the equivalent π- or T-circuit of any asymmetric unit cell, by cascading such circuits, it is possible to describe any infinite structure by means of symmetric unit cells by simply shifting the reference planes. However, in a physical periodic structure, it is not necessarily possible to identify a symmetric unit cell.

[15] An L-circuit can be considered a particular case of a T-circuit where one of the series impedances is null.

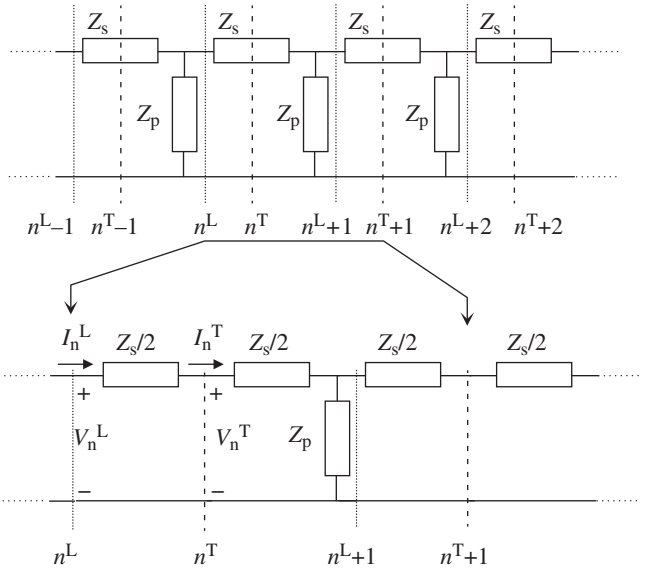

FIGURE 2.5 Periodic structure where the reference planes of the symmetric T-circuit unit cell (vertical dashed lines) and asymmetric L-circuit unit cell (vertical dotted lines) are indicated. The superscripts L or T in the port variables and reference planes are used to differentiate between the asymmetric and symmetric unit cells. Notice that the port currents do not vary by shifting the reference planes $\left(I_n^L = I_n^T\right)$, contrary to the port voltages $\left(V_n^L \neq V_n^T\right)$. To make the reference planes of the symmetric unit cells accessible, it suffices to split the series impedance into two identical impedances equal to $Z_s/2$.

$$B = Z_s + \frac{Z_s^2}{4Z_p} \tag{2.28b}$$

$$C = \frac{1}{Z_p} \tag{2.28c}$$

whereas the following parameters apply to the asymmetric unit cell:

$$A = 1 + \frac{Z_s}{Z_p} \tag{2.29a}$$

$$B = Z_s \tag{2.29b}$$

$$C = \frac{1}{Z_p} \tag{2.29c}$$

$$D = 1 \tag{2.29d}$$

Introducing the elements of (2.28) in (2.27), the Bloch impedance corresponding to the structure described by the symmetric unit cell is found to be

$$Z_B^{\pm} = \pm \frac{Z_s\left(1+\dfrac{Z_s}{4Z_p}\right)}{\sqrt{\left(1+\dfrac{Z_s}{2Z_p}\right)^2 - 1}} = \pm\sqrt{\frac{Z_s}{2}\left(\frac{Z_s}{2}+2Z_p\right)} \tag{2.30}$$

and it is real in the propagation regions if Z_s and Z_p are purely reactive impedances. For the structure composed by a cascade of the asymmetric L-circuit unit cells, the Bloch impedance is derived from (2.26) and (2.29)

$$Z_B^{\pm} = -\frac{2Z_s}{\dfrac{Z_s}{Z_p} \mp \sqrt{\left(2+\dfrac{Z_s}{Z_p}\right)^2 - 4}} = \pm\sqrt{\frac{Z_s}{2}\left(\frac{Z_s}{2}+2Z_p\right)} + \frac{Z_s}{2} \tag{2.31}$$

and it is a complex number in the region where wave propagation is allowed. As mentioned before, according to the usual definition of the positive current for forward and backward traveling waves, the two solutions of the Bloch impedance must be actually expressed as follows:

$$Z_B^{\pm} = \sqrt{\frac{Z_s}{2}\left(\frac{Z_s}{2}+2Z_p\right)} \pm \frac{Z_s}{2} \tag{2.32}$$

Expression (2.32) indicates that the real part of the Bloch impedance is identical to that of the symmetric structure (2.30), as expected. Notice that the imaginary part is the impedance that must be cascaded to the truncated periodic line ($+Z_s/2$ and $-Z_s/2$ in the load and source planes, respectively) in order to transform the finite asymmetric periodic structure to a symmetric network. Therefore, the complex Bloch impedance in the propagation regions of lossless asymmetric structures indicates that to match a load/source to the line it is necessary to series connect a reactive impedance, able to compensate the effects of asymmetry, plus the required resistive part, given by the absolute value of (2.30).

In the circuit of Figure 2.5, it is remarkable that the dispersion relation, given by (2.22), is insensitive to the position of the reference planes of the unit cell. Either by using the A and D parameters given by (2.28) or (2.29), expression (2.22) is found to be

$$\cos(\beta l) = 1 + \frac{Z_s}{2Z_p} \tag{2.33}$$

2.3.3 Effects of Asymmetry in the Unit Cell through an Illustrative Example

At this point, it is interesting to provide an example to illustrate the effects of asymmetry of the unit cell in the behavior of the structure. Let us consider the ladder network corresponding to the circuit model of a lossless conventional transmission line, where each unit cell describes a section of the transmission line that must be electrically short (Figure 2.6). For the symmetric unit cell, the Bloch impedance, inferred from (2.30), is

$$Z_{\mathrm{B}} = \sqrt{\frac{L}{C}\left(1-\frac{\omega^2}{\omega_{\mathrm{o}}^2}\right)} \tag{2.34}$$

where ω is the angular frequency, and $\omega_{\mathrm{o}} = 2/\sqrt{LC}$ is a cutoff frequency. Above this cutoff frequency, the Bloch impedance is purely imaginary, and propagation is not allowed. The network of Figure 2.6 is indeed a low-pass filter, whereas a lossless transmission line is an all-pass structure. The discrepancy is explained because the network of Figure 2.6, where L and C model the per-section inductance and capacitance of the transmission line, is valid at low frequencies (the wavelength must be much larger than the considered line section length). Nevertheless, for frequencies satisfying $\omega \ll \omega_{\mathrm{o}}$, the Bloch impedance coincides with the well-known characteristic impedance of the line (expression 1.9). For the asymmetric unit cell (L-network), the Bloch impedance, given by expression (2.32), is

$$Z_{\mathrm{B}}^{\pm} = \sqrt{\frac{L}{C}\left(1-\frac{\omega^2}{\omega_{\mathrm{o}}^2}\right)} \pm j\frac{1}{2}L\omega \tag{2.35}$$

As frequency decreases, the imaginary part of the Bloch impedance also decreases. Therefore, at sufficiently low frequencies, where $L\omega/2 << (L/C)^{1/2}$, the Bloch impedance that results by considering the asymmetric unit cell is essentially real. This means that in this frequency regime, the behavior of both terminated periodic structures (with cascaded symmetric and asymmetric unit cells) is expected to be similar. This has been verified by comparing the reflection and transmission coefficients (considering a source impedance of 50 Ω) of the 20-cell structures depicted in Figure 2.7, loaded with a resistance of value $R = (L/C)^{1/2} = 50\ \Omega$, which is a matched load at low

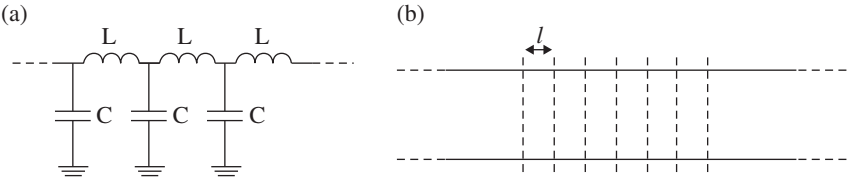

FIGURE 2.6 Model of a losses transmission line (a), where each unit cell describes the finite transmission line sections of length l (b).

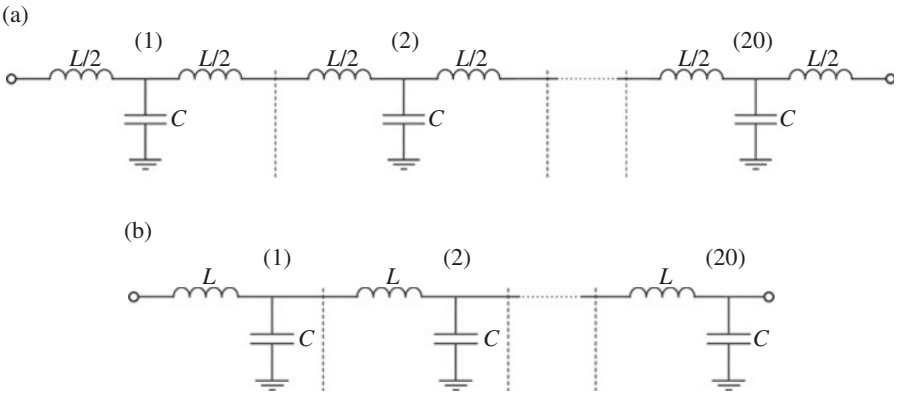

FIGURE 2.7 (a) Symmetric (T-circuit) and (b) asymmetric (L-circuit) networks modeling a 20-section lossless transmission line.

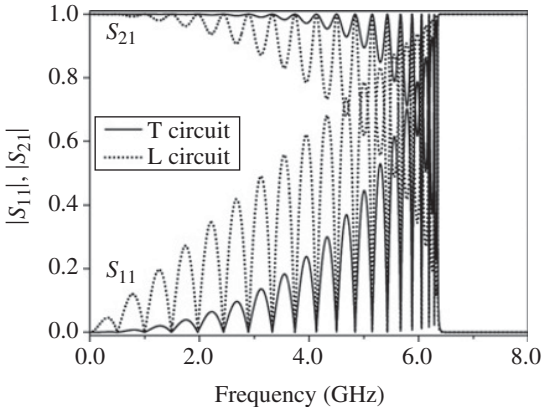

FIGURE 2.8 Reflection (S_{11}) and transmission (S_{21}) coefficients for the structures depicted in Figure 2.7 with $C = 1$ pF and $L = 2.5$ nH.

frequencies (see Fig. 2.8). As expected, at low frequencies all the injected power is delivered to the load ($|S_{11}| \ll 1$ and $|S_{21}| \cong 1$), and the reflection and transmission coefficients are similar for both structures. However, as frequency increases, the Bloch impedance varies and the structures are no longer matched to the source. The injected power is thus partially reflected back to the source (except at certain frequencies[16]), and above ω_o the lines are in the evanescent region, where $|S_{11}| \cong 1$ and

[16] Below the cut-off frequency, there are transmission peaks (reflection zeros) corresponding to phase matching. Namely, at these frequencies, the injected power is delivered to the load (despite that the line impedance is not matched to the ports) since the phase of the line is a multiple of 180°.

$|S_{21}| \ll 1$. However, the relevant aspect is that as frequency increases, both reflection coefficients and transmission coefficients progressively diverge as consequence of the increasing effects of the imaginary part of the Bloch impedance in the asymmetric periodic structure. If we force the imaginary part of (2.35) to be much smaller than the real part, that is,

$$\frac{1}{2}L\omega \ll \sqrt{\frac{L}{C}\left(1-\frac{\omega^2}{\omega_o^2}\right)} \tag{2.36}$$

the following condition is obtained:

$$\omega \ll \frac{1}{\sqrt{2}}\omega_o \tag{2.37}$$

which is indeed more restrictive (but comparable) than the necessary condition for the validity of the networks of Figure 2.7 as circuit models of a lossless transmission line ($\omega \ll \omega_o$). In summary, this analysis points out that in the long wavelength regime ($\lambda \gg l$), both terminated periodic structures of Figure 2.7 can be indistinctly used. This means that both networks are appropriate to describe or model a finite lossless transmission line. However, in general, this identification between the symmetric and asymmetric networks (which simply differ in the location of the reference planes – see Fig. 2.5) cannot be made. In other words, for a correct description of an actual periodic structure by means of a cascade of T- or π-sections, it is fundamental that such sections properly account for the possible asymmetries of the unit cell of the periodic structure (this aspect will be discussed in Chapter 3 in reference to asymmetric planar structures).

2.3.4 Comparison between Periodic Transmission Lines and Conventional Lines

It is important to mention that one-dimensional periodic structures, such as periodic loaded, or perturbed, transmission lines, can be characterized as if they were conventional transmission lines, that is, by means of a characteristic, or Bloch, impedance, and by means of a propagation constant.[17] However, as compared to conventional lines, where dispersion is absent (under ideal conditions), periodic transmission lines exhibit dispersion as well as pass bands and stop bands. Moreover, the Bloch impedance is frequency dependent, whereas the characteristic impedance of a conventional transmission line is solely dependent on the substrate characteristics and cross-sectional geometry of the line. Nevertheless, given a certain frequency in the region of propagation, periodically loaded or perturbed lines behave as conventional lines with identical propagation constant and characteristic impedance at the considered

[17] If the repeating period of the structure is asymmetric, caution must be taken due to the effects of termination.

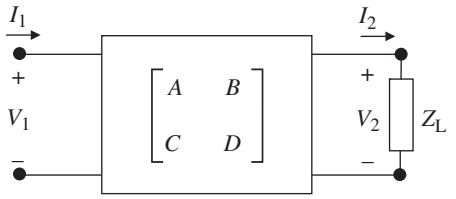

FIGURE 2.9 Arbitrary two-port network terminated with a load impedance Z_L.

frequency. Thus, for instance, if a periodic transmission line is terminated by a matched load at the considered frequency, that is, a load impedance identical to the Bloch impedance, all the injected power will be delivered to the load (as has been demonstrated in the example reported earlier and illustrated in Fig. 2.8—low-frequency region). Similarly, a finite periodic transmission line excited by a harmonic source and terminated by a load, exhibits identical behavior to that of a conventional line with identical electrical length and Bloch impedance. Specifically, if the electrical length of the periodic line is a multiple of π, the impedance seen from the source is the load impedance. These artificial lines based on periodic structures can also be used for the implementation of narrow band impedance or admittance inverters, by simply setting the Bloch impedance to the required impedance of the inverter at the design frequency, and the electrical length to $\pi/2$ or an odd multiple of $\pi/2$. Indeed, as will be demonstrated in Chapter 3, it is possible to implement impedance inverters by means of a single unit cell (of different type than those considered in this chapter), which is very interesting in terms of device miniaturization.

2.3.5 The Concept of Iterative Impedance

The characteristic impedance of a transmission line can also be defined as the load impedance necessary to "see" the same impedance from the source plane (or input port). In two-port networks, the impedance that satisfies the above requirement is called iterative impedance, Z_I.[18] For a given unit cell, the iterative impedance and the Bloch impedance are identical. To demonstrate this, let us consider that an arbitrary two-port network, described by the *ABCD* matrix, is loaded with an arbitrary impedance Z_L (Fig. 2.9). The voltage and current at the input port can be expressed as follows:

$$V_1 = AV_2 + B\frac{V_2}{Z_L} \tag{2.38a}$$

[18] Notice that the iterative impedance of an asymmetric network is different for ports 1 and 2 (similarly to the Bloch impedance for forward and backward travelling waves in such networks). The iterative impedance should not be confused with the image impedances of a two-port network. If we designate these image impedances as Z_{i1} and Z_{i2}, they satisfy (i) Z_{i1} is the input impedance at port 1 when port 2 is terminated with Z_{i2} and (ii) Z_{i2} is the input impedance at port 2 when port 1 is terminated with Z_{i1} [10]. However, for symmetric networks, the image impedances Z_{i1} and Z_{i2} are identical and coincide with the iterative impedance and Bloch impedance.

$$I_1 = CV_2 + D\frac{V_2}{Z_L} \tag{2.38b}$$

Hence, the input impedance is

$$Z_{in} = \frac{V_1}{I_1} = \frac{A + B/Z_L}{C + D/Z_L} \tag{2.39}$$

If $Z_L = Z_I$, then $Z_{in} = Z_I$, and Z_I can be isolated from (2.39), giving

$$Z_I = \frac{A - D \pm \sqrt{(A+D)^2 - 4}}{2C} \tag{2.40}$$

Although apparently expressions (2.40) and (2.26) are different, simple algebra demonstrates that $Z_B = Z_I$, as anticipated before. Namely, (2.26) can be expressed as follows:

$$Z_B^{\pm} = -\frac{2B}{A - D \mp \sqrt{(A+D)^2 - 4}} \cdot \frac{A - D \pm \sqrt{(A+D)^2 - 4}}{A - D \pm \sqrt{(A+D)^2 - 4}} \tag{2.41}$$

which gives

$$Z_B^{\pm} = \frac{2B\left(A - D \pm \sqrt{(A+D)^2 - 4}\right)}{4(AD - 1)} = \frac{A - D \pm \sqrt{(A+D)^2 - 4}}{2C} = Z_I \tag{2.42}$$

where the reciprocity condition $AD - BC = 1$ has been used. Indeed, the term "iterative impedance" is usually restricted to two-port networks with few (or even a single) unit cells, where the propagation of Bloch waves as traveling waves with several wavelengths is not possible. However, it is important to clarify that expressions (2.21) and (2.26) are valid regardless of the number of cells (they are valid even for a single-cell structure). Throughout this book, the terms Bloch impedance and characteristic impedance, in reference to artificial transmission lines, are considered to be synonymous.

2.4 COUPLED MODE THEORY[19]

As anticipated in the introduction, the specific periodic structures that will be analyzed in this chapter are transmission lines loaded with reactive elements, and nonuniform planar transmission lines, namely, transmission lines with periodic perturbation in the conductor strip width or in the ground plane. For the latter case, the coupled mode

[19] This section has been co-authored with Txema Lopetegi (Public University of Navarre, Spain).

theory, and specifically the cross-section method, is a very useful analysis tool [11–15]. It is a complementary approach to the transfer matrix method, able to provide detailed information (under several reasonable approximations) on the main parameters of the periodic nonuniform transmission line, such as the S-parameters, the central frequencies of the stop bands as well as their rejection level and bandwidth, the harmonic content, and so on.

2.4.1 The Cross-Section Method and the Coupled Mode Equations

The basic idea of the cross-section method is that the electromagnetic (EM) fields at any cross section of a nonuniform transmission line can be expressed as a superposition of the forward and backward traveling waves associated to the different modes of an auxiliary (or reference) uniform transmission line with the same cross section as the considered cross section of the nonuniform transmission line.[20] Namely,

$$\Psi = \sum_i a_i \Psi^i + \sum_i \int_0^\infty a_i(k_t)\Psi^i(k_t)dk_t \tag{2.43}$$

where Ψ is either the total electric or magnetic field of the nonuniform transmission line, Ψ^i is the field pattern of the ith discrete mode of the auxiliary uniform transmission line, and a_i are the corresponding weights, or coefficients, which can be interpreted as the complex amplitudes of the discrete modes along the non-uniform transmission line, and are only function of z (the propagation direction) and frequency. Notice that expression (2.43) gives the field expansion of an open transmission line (or waveguide) where, besides the discrete modes, a system of modes with a continuous spectrum is also included (second term of the right-hand side of 2.43). This additional system is in general necessary since the radiated field cannot be represented by the discrete modes. Conversely, in a closed waveguide, the discrete modes (including the propagating and evanescent modes) form a complete and orthogonal system.[21] The coefficients of the above field expansion satisfy a system of integrodifferential equations, known as coupled mode equations. The derivation of the coupled mode equations for the general case of open transmission lines (or waveguides) is not straightforward and is out of the scope of this book (the authors recommend Refs. [12–14] to the interested readers). The interest in this book is to infer simplified coupled mode equations of practical use for the analysis of the considered structures by applying reasonable approximations to the general equations. Thus, the starting

[20] This includes the same permeability and permittivity distributions for nonhomogeneous substrates. Nevertheless, only artificial transmission lines implemented on homogeneous substrates are considered in this book.

[21] The modes of a closed waveguide can be enumerated by a subscript, and the set is composed by an infinite number of discrete modes. However, in an open waveguide, the system of discrete modes is formed by a finite number of modes, all of them in propagation.

point is the expression of the general integrodifferential coupled mode equations that, for an open transmission line or waveguide nonuniform in the propagation direction, take the form[22]:

$$\frac{da_m}{dz} + j\beta_m a_m = \sum_i a_i C_{mi} + \sum_i \int_0^\infty a_i(k_t) C_{mi}(k_t) dk_t \tag{2.44a}$$

$$\frac{da_n\left(\widetilde{k}_t\right)}{dz} + j\beta_n\left(\widetilde{k}_t\right) a_n\left(\widetilde{k}_t\right) = \sum_i a_i C_{ni}^{c}\left(\widetilde{k}_t\right) + \sum_i \int_0^\infty a_i(k_t) C_{ni}^{c}\left(\widetilde{k}_t, k_t\right) dk_t \tag{2.44b}$$

where β_m is the phase constant of the mth discrete mode, C_{mi} is the coupling coefficient between the mth and ith discrete modes, and $\beta_n(k_t)$, $C_{mi}(k_t)$, $C_{ni}^{c}\left(\widetilde{k}_t\right)$, and $C_{ni}^{c}\left(\widetilde{k}_t, k_t\right)$ are the corresponding parameters for the continuous spectrum modes (their expressions can be found in Ref. [14]), and

$$k_t^2 = k_o^2 - \beta_i^2(k_t) \tag{2.45}$$

with $k_0 = \omega\sqrt{\mu_o \varepsilon_o}$, and $\beta_i(k_t) = +\sqrt{k_0^2 - k_t^2}$ for $i > 0$, $\beta_i(k_t) = -\sqrt{k_0^2 - k_t^2}$ for $i < 0$. There is one of these coupled mode equations for each mode, including their forward (+) and backward (−) traveling waves.

Expression (2.44a and b) can be substantially simplified if several assumptions are made:

- The first one is to neglect the coupling of energy to the modes of the continuous spectrum. This is reasonable if the considered structures have little radiation losses in the considered frequency bands (however, the continuous spectrum cannot be neglected in applications where devices are designed to radiate, i.e., antennas). This approximation notably simplifies the coupled mode equations since expression (2.44b) can be ignored, and the second term of the right-hand side of (2.44a) has a negligible effect as well.
- The second approximation consists of assuming single-mode operation, that is, the fundamental mode with two associated waves: the forward and backward traveling waves. In structures with periodic defects or patterns in the ground plane, further modes may appear. For instance, in microstrip lines with slots

[22] For the derivation of these equations, it is also assumed that the nonuniform transmission lines are lossless.

in the ground plane, a quasimicrostrip mode[23] and a quasislot mode are possible (at moderate frequencies and for conventional microwave substrate thicknesses, higher-order modes are not present). However, if the periodic microstrip structure is excited by a pure microstrip line, the corresponding mode (quasi-TEM mode) has very small correlation with the quasislot mode, and strong correlation with the quasimicrostrip mode. Therefore, the quasislot mode can be neglected, and single-mode operation is justified.

With the previous approximations, the system of coupled mode equations simplifies to [14, 16]

$$\frac{da^+}{dz} + j\beta^+ a^+ = a^+ C^{++} + a^- C^{+-} \tag{2.46a}$$

$$\frac{da^-}{dz} + j\beta^- a^- = a^- C^{--} + a^+ C^{-+} \tag{2.46b}$$

where the subscripts (+) and (−) designate the forward and backward traveling waves, respectively, associated to the fundamental TEM or quasi-TEM mode. Expression (2.46a and b) can be further simplified to

$$\frac{da^+}{dz} + j\beta a^+ = a^- K \tag{2.47a}$$

$$\frac{da^-}{dz} - j\beta a^- = a^+ K \tag{2.47b}$$

where the fundamental property that the phase constants of the forward and backward traveling wave of a discrete mode are identical except the sign ($\beta^+ = -\beta^- = \beta$) has been used. With regard to the coupling coefficients, notice that due to symmetry considerations, $C^{+-} = C^{-+} \equiv K$. Moreover, $C^{--} = C^{++} = 0$ since the coupled mode Equations 2.46a and 2.46b must give trivial solutions of the form $a^+ \propto e^{-j\beta z}$ and $a^- \propto e^{+j\beta z}$, for the case of a lossless uniform transmission line (where $K = 0$). Expression (2.47a and 2.47b) can thus be expressed in the following compact form:

$$\frac{d}{dz}\begin{bmatrix} a^+ \\ \\ a^- \end{bmatrix} = \begin{bmatrix} -j\beta & K \\ \\ K & j\beta \end{bmatrix} \cdot \begin{bmatrix} a^+ \\ \\ a^- \end{bmatrix} \tag{2.48}$$

[23] By quasimicrostrip mode, we mean the fundamental mode of the line when a defect in the form of a slot in the ground plane is present.

where a single coupling coefficient, K, between the forward and backward traveling waves associated to the fundamental TEM or quasi-TEM mode, plus the phase constant of the auxiliary uniform waveguide, characterize the structure. Notice that both the phase constant and the coupling coefficient are functions of z and frequency, that is, $\beta = \beta(z,\omega)$ and $K = K(z,\omega)$. The phase constant of the operation mode can be calculated as

$$\beta(z,\omega) = \frac{\omega}{c}\sqrt{\varepsilon_{\mathrm{re}}(z,\omega)} \tag{2.49}$$

where the explicit dependence of the effective dielectric constant, defined in Chapter 1, on z and ω has been introduced in the square root in order to highlight that, rather than being an averaged dielectric constant, the effective dielectric constant varies with the cross section, which in turn depends on the position along the propagation axis in a nonuniform transmission line. The effective dielectric constant at each cross section (i.e., that of the auxiliary uniform transmission line), and hence the phase constant, can be numerically calculated [10, 17], or inferred by means of most available EM solvers.

The exact expression of the coupling coefficient involves the calculation of the fields of the modes in the auxiliary uniform transmission line associated to the cross section of interest (which varies with z) [14]. Nevertheless, the coupling coefficient can be approximated by a simple expression that depends only on the characteristic impedance, Z_o, of the transmission line according to (see Appendix E):

$$K(z,\omega) = -\frac{1}{2Z_o}\frac{dZ_o}{dz} \tag{2.50}$$

In microstrip or coplanar waveguide transmission lines with periodic perturbation in the conductor strip, Z_o can be point-to-point obtained along the propagation axis by means of available transmission line calculators. If the ground plane is etched, for instance, by periodically drilling holes underneath the conductor strip of a microstrip line (a usual technique for the implementation of EBG-based reflectors [18, 19]), the calculation of Z_o is not so straightforward. Nonetheless, the impedance of expression (2.50) must be inferred from the power and current carried by the mode according to

$$Z_o(z,\omega) = 2\frac{P^+}{|I^+|^2} \tag{2.51}$$

Indeed, the dependence of Z_o with frequency can be neglected to a first-order approximation as it is customarily done in planar transmission lines.

The matrix equation (2.48) is a system of first-order linear differential equations. In order to solve these equations, it is necessary to define the z interval corresponding to

the structure under study, delimited by $z = 0$ and $z = L$ (the device length), and appropriate boundary conditions. Such boundary conditions depend on how the ports of the structure are loaded. Typically, the output port is loaded with a matched load, whereas a unitary excitation is applied at the input of the device. Under these conditions, the following boundary values apply:

$$a^+(z=0) = a_{\text{in}}^+ = 1 \tag{2.52a}$$

$$a^-(z=L) = a_{\text{out}}^- = 0 \tag{2.52b}$$

and the coupled mode equations can be easily solved through numerical methods.

2.4.2 Relation between the Complex Mode Amplitudes and S-Parameters

Once the complex amplitudes $a^+(z,\omega)$ and $a^-(z,\omega)$ are inferred, the S-parameters of the device can be straightforwardly calculated. According to the definitions of these parameters, given in Appendix C,

$$S_{11} = \left.\frac{b_1}{a_1}\right|_{a_2=0} = \left.\frac{V_1^- \sqrt{Z_o}}{V_1^+ \sqrt{Z_o}}\right|_{a_2=0} \tag{2.53a}$$

$$S_{21} = \left.\frac{b_2}{a_1}\right|_{a_2=0} = \left.\frac{V_2^- \sqrt{Z_o}}{V_1^+ \sqrt{Z_o}}\right|_{a_2=0} \tag{2.53b}$$

$$S_{22} = \left.\frac{b_2}{a_2}\right|_{a_1=0} = \left.\frac{V_2^- \sqrt{Z_o}}{V_2^+ \sqrt{Z_o}}\right|_{a_1=0} \tag{2.53c}$$

$$S_{12} = \left.\frac{b_1}{a_2}\right|_{a_1=0} = \left.\frac{V_1^- \sqrt{Z_o}}{V_2^+ \sqrt{Z_o}}\right|_{a_1=0} \tag{2.53d}$$

where Z_o is the reference impedance of the ports (it is assumed that both ports have the same impedance), and $z = 0$ and $z = L$ are the reference planes of the input (1) and output (2) ports, respectively. The relations between the voltages associated to the incident (V_1^+, V_2^+) and reflected (V_1^-, V_2^-) waves from the ports and those associated to the forward V^+ and backward V^- traveling waves are as follows:

$$V_1^+ = V^+(z=0) \tag{2.54a}$$

$$V_1^- = V^-(z=0) \tag{2.54b}$$

$$V_2^+ = V^-(z=L) \tag{2.54c}$$

$$V_2^- = V^+(z=L) \tag{2.54d}$$

On the other hand, the voltages associated to the forward V^+ and backward V^- traveling waves must be proportional to the complex amplitudes according to[24]

$$V^+ = Ca^+ \tag{2.55a}$$

$$V^- = Ca^- \tag{2.55b}$$

Therefore, using (2.54) and (2.55), the S-parameters can be expressed as follows:

$$S_{11} = \left.\frac{Ca^-(z=0)}{Ca^+(z=0)}\right|_{a^-(z=L)=0} = \left.\frac{a^-(z=0)}{a^+(z=0)}\right|_{a^-(z=L)=0} \tag{2.56a}$$

$$S_{21} = \left.\frac{Ca^+(z=L)}{Ca^+(z=0)}\right|_{a^-(z=L)=0} = \left.\frac{a^+(z=L)}{a^+(z=0)}\right|_{a^-(z=L)=0} \tag{2.56b}$$

$$S_{22} = \left.\frac{Ca^+(z=L)}{Ca^-(z=L)}\right|_{a^+(z=0)=0} = \left.\frac{a^+(z=L)}{a^-(z=L)}\right|_{a^+(z=0)=0} \tag{2.56c}$$

$$S_{12} = \left.\frac{Ca^-(z=0)}{Ca^-(z=L)}\right|_{a^+(z=0)=0} = \left.\frac{a^-(z=0)}{a^-(z=L)}\right|_{a^+(z=0)=0} \tag{2.56d}$$

Hence, by solving the coupled mode equations with the boundary conditions given by (2.52), the S-parameters can be inferred using (2.56).

[24] The proportionality between the voltages and complex amplitudes of the forward and backward travelling waves can be alternatively expressed as $V^+ = Ca^+$ and $V^- = -Ca^-$. The (–) or (+) sign in the second expression simply depends on the relations between the (x,y) dependent part of the fields of the forward and backward travelling waves. The (+) sign (i.e., 2.55) results when such relations are taken as $E_x^- = E_x^+ ; E_y^- = E_y^+ ; E_z^- = -E_z^+$ for the electric fields, and as $H_x^- = -H_x^+ ; H_y^- = -H_y^+ ; H_z^- = H_z^+$ for the magnetic fields, following [11, 15]. The (–) sign is obtained if the fields are chosen to satisfy $E_x^- = -E_x^+ ; E_y^- = -E_y^+ ; E_z^- = E_z^+$ and $H_x^- = H_x^+ ; H_y^- = H_y^+ ; H_z^- = -H_z^+$, following [13, 14]. Notice that if the (–) sign is chosen in (2.55b), a (–) sign would appear in (2.56a) and (2.56c), with the result of a more unfamiliar expression for S_{11} and S_{22}. However, this change in the relation between the fields of the forward and backward travelling waves implies also a change in the sign of the coupling coefficient K. Notice that the change of sign in K and a^- (necessary to leave the S-parameters unaltered) keeps invariant the coupled mode equations (2.48).

2.4.3 Approximate Analytical Solutions of the Coupled Mode Equations

Solving the system of coupled mode equations (2.48) requires in general a numerical method. However, by considering a pair of additional approximations (valid in most cases of practical interest), it is possible to further simplify the equations in such a way that analytical solutions can be obtained, and, from them, relevant parameters of EBG-based planar transmission lines[25] can be inferred. Such needed approximations are [14]:

- The z dependence of the phase constant β (or ε_{re}) is neglected. This means that an averaged value of β (and ε_{re}) must be chosen. As justified in Appendix F, the most adequate value is:

$$\varepsilon_{re} = \left(\frac{1}{l} \int_0^l \sqrt{\varepsilon_{re}(z)} \cdot dz \right)^2 \tag{2.57}$$

  where l is the period of the EBG-based structure.
- The analysis is restricted to a range of frequencies in the vicinity of the central frequency of a certain (nth) rejected band.[26] This approximation is necessary in order to express the coupled mode equations in terms of the nth coefficient of the Fourier expansion of the coupling coefficient, $K(z)$, which is a periodic function of z if the nonuniformity of the transmission line is also periodic.[27]

Let us now see how the previous approximations notably simplify the coupled mode equations. Due to periodicity, the coupling coefficient can be expanded in a Fourier series as follows:

$$K(z) = \sum_{n=-\infty}^{n=+\infty} K_n e^{j\frac{2\pi n}{l} z} \tag{2.58}$$

which in turn can be expressed as follows:

$$K(z) = \sum_{n=1}^{n=+\infty} |2K_n| \cos\left(\frac{2\pi n}{l} z + \arg(K_n) \right) \tag{2.59}$$

[25] As already mentioned in the introduction of this chapter, by EBG-based planar transmission lines, we mean nonuniform periodic lines with either modulation of the conductor strip or ground plane etching.

[26] In general, periodic EBG-based transmission lines exhibit multiple rejection bands, as results from the Floquet analysis of Section 2.2.

[27] Notice that the period of $K(z)$ is also l.

since $K(z)$ is a real function (i.e., $K_{-n} = K_n^{\,*} = |K_n| \cdot e^{-j\arg(Kn)}$), and $K_0 = 0$ (the mean value of the coupling coefficient of a periodic structure is null). Let us now express the complex amplitudes as a function of the averaged β as follows [14]:

$$a^+(z) = A^+(z) \cdot e^{-j\beta z} \tag{2.60a}$$

$$a^-(z) = A^-(z) \cdot e^{+j\beta z} \tag{2.60b}$$

Using these variables, the coupled mode equations can be written as

$$\frac{dA^+}{dz} = K(z) \cdot A^- \cdot e^{+j2\beta z} \tag{2.61a}$$

$$\frac{dA^-}{dz} = K(z) \cdot A^+ \cdot e^{-j2\beta z} \tag{2.61b}$$

and introducing (2.58) in (2.61), the following equations result:

$$\frac{dA^+}{dz} = \sum_{n=1}^{\infty} \left(K_n \cdot e^{+j2\left(\beta + \frac{n\pi}{l}\right)z} + K_{-n} \cdot e^{+j2\left(\beta - \frac{n\pi}{l}\right)z} \right) \cdot A^- \tag{2.62a}$$

$$\frac{dA^-}{dz} = \sum_{n=1}^{\infty} \left(K_n \cdot e^{-j2\left(\beta - \frac{n\pi}{l}\right)z} + K_{-n} \cdot e^{-j2\left(\beta + \frac{n\pi}{l}\right)z} \right) \cdot A^+ \tag{2.62b}$$

For the solution of Equations 2.62 over the whole frequency spectrum, it is necessary to keep all the coefficients, K_n, of the series expansion of $K(z)$, unless some of them are negligible or null.[28] However, for frequencies in the vicinity of those frequencies satisfying

$$\beta = \frac{n\pi}{l} \tag{2.63}$$

only one term in the summations of (2.62) is significant; namely, the term K_{-n} in (2.62a), and the term K_n in (2.62b). The reason is that the corresponding exponential has an argument close to zero for these terms, giving a significant contribution to the sum. For the other terms, the exponentials are rapidly varying functions of z, and when these terms, multiplied by A^-, or A^+ (which are slowly varying functions of z), are integrated over several periods, their contribution is negligible. From a physical point

[28] Notice, for instance, that for a sinusoidal variation of $K(z)$, all the coefficients of the series are null, except $K_{\pm 1}$.

of view, this means that at those frequencies satisfying (2.63), a strong coupling (and hence an important transfer of energy) between the forward and backward traveling waves is expected. This energy transfer gives rise to significant reflection of the injected power, with the result of stop bands in the frequency response, caused by the perturbation. Notice that condition (2.63), usually known as phase matching, or resonant coupling, is equivalent to expression (2.9). Therefore, the coupling equations (2.62) provide the mathematical explanation for the presence of band gaps in artificial transmission lines based on periodic structures. Notice that at frequencies far enough from those frequencies satisfying phase matching, all the terms in the right-hand side of (2.62) experiment quick variations with z. When such terms are multiplied by A^- (in 2.62a) or A^+ (in 2.62b), and are integrated over a distance much larger than the period l, their contributions tend to vanish, and A^- and A^+ tend to be constant. Indeed, if the boundary conditions (2.52) are applied, and the considered frequencies are within the pass band regions, we expect that the solutions of (2.62) can be approximated by $A^+(z) = 1$ and $A^-(z) = 0$ (or $a^+(z) = e^{-j\beta z}$ and $a^-(z) = 0$), corresponding to roughly total transmission between the input and output ports. Notice that if $A^-(z) = 0$, it directly results from (2.62a) that $A^+(z)$ is constant with z, and (2.62b) gives a negligible value of $A^-(z)$ if the number of periods of the structure is large enough, this being consistent with our previous prediction.

According to the previous analysis, for the frequency range in the vicinity of the nth rejected frequency band; and for a periodic structure with total length satisfying $L >> l$, the coupled mode equations can be simplified to

$$\frac{dA^+}{dz} = K_n^* \cdot A^- \cdot e^{+j2\Delta\beta z} \tag{2.64a}$$

$$\frac{dA^-}{dz} = K_n \cdot A^+ \cdot e^{-j2\Delta\beta z} \tag{2.64b}$$

where

$$\Delta\beta = \beta - \frac{n\pi}{l} \tag{2.65}$$

$\Delta\beta$ being null at the frequency satisfying the phase matching condition. To solve (2.64), let us express the weighting factors of the coupling coefficient as

$$K_n = jk \tag{2.66}$$

The coupling equations can thus be written as

$$\frac{dA^+}{dz} = -jk^* \cdot A^- \cdot e^{+j2\Delta\beta z} \tag{2.67a}$$

$$\frac{dA^-}{dz} = jk \cdot A^+ \cdot e^{-j2\Delta\beta z} \tag{2.67b}$$

In order to solve the previous equations analytically, the following new variables are introduced [14, 20]:

$$R(z) = A^+(z) \cdot e^{-j\Delta\beta z} = a^+(z) e^{j\frac{\pi}{l}z} \tag{2.68a}$$

$$S(z) = A^-(z) \cdot e^{j\Delta\beta z} = a^-(z) e^{-j\frac{\pi}{l}z} \tag{2.68b}$$

and the coupled mode equations can be written as follows:

$$\frac{dR}{dz} = -j\Delta\beta \cdot R - jk^* \cdot S \tag{2.69a}$$

$$\frac{dS}{dz} = j\Delta\beta \cdot S + jk \cdot R \tag{2.69b}$$

The general solutions of (2.69) are of the form[29]:

$$R(z) = R^+ \cdot e^{-\gamma z} + R^- \cdot e^{\gamma z} \tag{2.70a}$$

$$S(z) = S^+ \cdot e^{-\gamma z} + S^- \cdot e^{\gamma z} \tag{2.70b}$$

where

$$\gamma = +\sqrt{|k|^2 - (\Delta\beta)^2} \tag{2.71}$$

Let us now introduce boundary conditions compatible with (2.52), namely, a matched output port. This means that $a^-(z = L) = S(z = L) = 0$, and, using (2.70b), it follows that $S^+ = -S^- \cdot e^{2\gamma L}$. Therefore, $S(z)$ can be expressed as

$$S(z) = S^+ \cdot e^{-\gamma z}\left(1 - e^{-2\gamma(L-z)}\right) \tag{2.72}$$

[29] The calculation of the general solutions of (2.69) is not straightforward. To demonstrate that (2.70), with γ given by (2.71), are the general solutions of (2.69), we first introduce (2.70) in (2.69). This gives two equations where all the terms are multiplied either by $e^{\gamma z}$ or $e^{-\gamma z}$. By equating the corresponding weights of these exponentials, four linear equations in the variables S^+, S^-, R^+ and R^-, which can be expressed in matrix form, are obtained. For a non-trivial solution, it is necessary that the associated determinant is null, and this occurs if (2.71) is satisfied.

and introducing (2.72) in (2.69b), $R(z)$ is found to be

$$R(z) = -\frac{S^+ e^{-\gamma z}}{jk} \cdot \left\{ \gamma \left(1 + e^{-2\gamma(L-z)} \right) + j\Delta\beta \left(1 - e^{-2\gamma(L-z)} \right) \right\} \tag{2.73}$$

Assuming an incident wave at the input port $R(z=0) = R_o$, the integration constant S^+ can be obtained, and expressions (2.72) and (2.73), after some tedious calculations, are found to be

$$R(z) = -\frac{R_o \{ \Delta\beta \sinh(\gamma(z-L)) + j\gamma \cosh(\gamma(z-L)) \}}{\Delta\beta \sinh(\gamma L) - j\gamma \cosh(\gamma L)} \tag{2.74a}$$

$$S(z) = \frac{R_o k \sinh(\gamma(z-L))}{\Delta\beta \sinh(\gamma L) - j\gamma \cosh(\gamma L)} \tag{2.74b}$$

Finally, from (2.68), the solutions of the coupled mode equations (2.47a and 2.47b) under the considered approximations are

$$a^+(z) = -\frac{\{ \Delta\beta \sinh(\gamma(z-L)) + j\gamma \cosh(\gamma(z-L)) \}}{\Delta\beta \sinh(\gamma L) - j\gamma \cosh(\gamma L)} a^+(0) \cdot e^{-j\frac{\pi z}{l}} \tag{2.75a}$$

$$a^-(z) = \frac{k \sinh(\gamma(z-L))}{\Delta\beta \sinh(\gamma L) - j\gamma \cosh(\gamma L)} a^+(0) \cdot e^{j\frac{\pi z}{l}} \tag{2.75b}$$

Notice that the above expressions are the approximate solutions of the coupled equations for a periodic EBG structure with length L, with input and output ports placed at $z = 0$ and $z = L$, respectively, and excited by an incident wave $a^+(z=0) = a^+(0)$, and with the output port matched, that is, $a^-(z=L) = 0$. Once the approximate solutions of the complex amplitudes $a^+(z)$ and $a^-(z)$ are known, the S-parameters can be inferred using (2.56). This gives

$$S_{11} = \left. \frac{a^-(z=0)}{a^+(z=0)} \right|_{a^-(z=L)=0} = \frac{k \sinh(\gamma L)}{-\Delta\beta \sinh(\gamma L) + j\gamma \cosh(\gamma L)} \tag{2.76a}$$

$$S_{21} = \left. \frac{a^+(z=L)}{a^+(z=0)} \right|_{a^-(z=L)=0} = \frac{j\gamma \cdot e^{-j\frac{\pi L}{l}}}{-\Delta\beta \sinh(\gamma L) + j\gamma \cosh(\gamma L)} \tag{2.76b}$$

In order to obtain S_{12} and S_{22}, it is necessary to modify the boundary conditions. In this case, the input port is matched, and hence $a^+(z=0) = R(z=0) = 0$. Therefore, using (2.70a), it follows that $R^+ = -R^-$, and $R(z)$ can be expressed as

$$R(z) = R^{+}\left(e^{-\gamma z} - e^{\gamma z}\right) = -2R^{+}\sinh(\gamma z) \tag{2.77}$$

Introducing (2.77) in (2.69a), $S(z)$ is found to be

$$S(z) = \frac{2R^{+}}{jk^{*}} \cdot \{\gamma\cosh(\gamma z) + j\Delta\beta\sinh(\gamma z)\} \tag{2.78}$$

As proceeded before, in order to determine the integration constant R^{+}, it is necessary to set the incident wave at the output port to $S(z = L) = S_{\mathrm{o}}$. Substituting the resulting value in (2.77) and (2.78), we obtain

$$R(z) = -\frac{S_{\mathrm{o}}k^{*}\sinh(\gamma z)}{\Delta\beta\sinh(\gamma L) - j\gamma\cosh(\gamma L)} \tag{2.79a}$$

$$S(z) = \frac{S_{\mathrm{o}}\{\Delta\beta\sinh(\gamma z) - j\gamma\cosh(\gamma z)\}}{\Delta\beta\sinh(\gamma L) - j\gamma\cosh(\gamma L)} \tag{2.79b}$$

and using (2.68),

$$a^{+}(z) = \frac{k^{*}\sinh(\gamma z)}{\Delta\beta\sinh(\gamma L) - j\gamma\cosh(\gamma L)} a^{-}(L)\cdot e^{-j\frac{n\pi}{l}(z+L)} \tag{2.80a}$$

$$a^{-}(z) = -\frac{\{\Delta\beta\sinh(\gamma z) - j\gamma\cosh(\gamma z)\}}{\Delta\beta\sinh(\gamma L) - j\gamma\cosh(\gamma L)} a^{-}(L)\cdot e^{+j\frac{n\pi}{l}(z-L)} \tag{2.80b}$$

where $a^{-}(L) = S_{\mathrm{o}}e^{+jn\pi L/l}$. Finally, using (2.56), S_{22} and S_{12} are found to be

$$S_{22} = \left.\frac{a^{+}(z=L)}{a^{-}(z=L)}\right|_{a^{+}(z=0)=0} = \frac{k^{*}\sinh(\gamma L)\cdot e^{-j\frac{2n\pi}{l}L}}{-\Delta\beta\sinh(\gamma L) + j\gamma\cosh(\gamma L)} \tag{2.81a}$$

$$S_{12} = \left.\frac{a^{-}(z=0)}{a^{-}(z=L)}\right|_{a^{+}(z=0)=0} = \frac{j\gamma\cdot e^{-j\frac{n\pi}{l}L}}{-\Delta\beta\sinh(\gamma L) + j\gamma\cosh(\gamma L)} \tag{2.81b}$$

Notice that $S_{12} = S_{21}$, and the S-parameters satisfy the unitarity conditions, as expected for reciprocal and lossless networks.

Inspection of (2.75) and (2.80) indicates that the z-dependent part of the wave solutions is an exponential with phase constants given by [3, 14, 21]

$$\beta' = \frac{n\pi}{l} \pm j\gamma = \frac{n\pi}{l} \pm j\sqrt{|k|^{2} - (\Delta\beta)^{2}} \tag{2.82a}$$

for the forward traveling wave, $a^{+}(z)$, and

$$\beta' = -\frac{n\pi}{l} \pm j\gamma = -\frac{n\pi}{l} \pm j\sqrt{|k|^2 - (\Delta\beta)^2} \tag{2.82b}$$

for the backward traveling wave, $a^{-}(z)$. Therefore β' is the approximate phase constant of the Bloch waves of the periodic structure. Notice that for $|\Delta\beta| < |k|$, the phase constant has an imaginary part. This region is the forbidden band (bandgap) of the periodic structure. On the contrary, far enough from the phase matching condition ($|\Delta\beta| > |k|$), β' is real and the structure is transparent. In the limit of small perturbations ($k \cong 0$), and for sufficiently large values of $|\Delta\beta|$ (i.e., $|\Delta\beta| >> |k|$), the phase constant can be approximated by

$$\beta' = \frac{n\pi}{l} \pm \Delta\beta\sqrt{1 - \frac{|k|^2}{(\Delta\beta)^2}} \approx \frac{n\pi}{l} \pm \Delta\beta = \frac{n\pi}{l} \pm \left(\beta - \frac{n\pi}{l}\right) = \beta, \text{ or } -\beta + \frac{2n\pi}{l} \tag{2.83a}$$

or

$$\beta' \approx -\frac{n\pi}{l} \pm \Delta\beta = -\frac{n\pi}{l} \pm \left(\beta - \frac{n\pi}{l}\right) = -\beta, \text{ or } \beta - \frac{2n\pi}{l} \tag{2.83b}$$

which is coherent with (2.6). Notice, however, that in (2.83) there are only four terms: the fundamental (forward or backward traveling), and those space harmonics with index $\pm n$. This is expected since this analysis is valid for frequencies in the vicinity of the nth forbidden band.

In order to obtain a more accurate solution for the phase constant of the fundamental space harmonic (notice that 2.82 gives an approximate solution), it is necessary to calculate the complex amplitudes $a^{+}(z)$ and $a^{-}(z)$ numerically, and, from them, the S-parameters. Using the transformations (C.22), the *ABCD* matrix can be inferred, and the dispersion relation can be finally derived from (2.22).

2.4.4 Analytical Expressions for Relevant Parameters of EBG Periodic Structures

Apart from the S-parameters, there are other relevant parameters of interest in EBG one-dimensional periodic structures such as the frequency of maximum reflectivity, the value of this maximum reflectivity, and the bandwidth of the frequency band where significant reflection is achieved. The purpose of this subsection is to provide analytical expressions for these parameters [14, 16, 22].

The frequency of maximum reflectivity, $f_{\max}$, is that frequency satisfying $\Delta\beta = 0$, or $\beta_{\max} = n\pi/l$. Therefore,

$$f_{\max} = n\frac{c}{2l\sqrt{\varepsilon_{re}}} \tag{2.84}$$

where c is the speed of light in vacuum. Notice that if $\Delta\beta = 0$, then $\gamma = |k|$, and the value of maximum reflectivity (from 2.76a and 2.81a) is

$$|S_{11}|_{\max} = |S_{22}|_{\max} = \tanh(|k|L) \tag{2.85}$$

Notice that $|S_{11}|_{\max} = |S_{22}|_{\max} \to 1$ (i.e., 0 dB) as $|k|L \to \infty$. From 2.76b and 2.81b, the maximum attenuation (minimum transmission) is found to be

$$|S_{21}|_{\min} = |S_{12}|_{\min} = \operatorname{sech}(|k|L) \tag{2.86}$$

It is important at this point to analyze the dependence of the maximum reflectivity, or minimum transmission, with the parameters of the EBG periodic structure. Notice that, as expected, the value of maximum reflectivity depends on the magnitude of the periodic perturbation through $|k|$, which is the modulus of the considered K_n term of the Fourier series expansion of the coupling coefficient (see expressions 2.58 and 2.59). The larger the periodic perturbation, the higher the derivative of the characteristic impedance and hence the amplitude of the coupling coefficient given by (2.50). Thus, increasing the magnitude of the perturbation has the effect of increasing the terms of the series expansion of $K(z)$. On the other hand, an increase in device length, L, means that the structure includes an increasing number of periods, with the effect of more power being transferred to the backward traveling waves and hence more reflection.

Concerning the reflected bandwidth, it is reasonable to consider that it is given by the frequency range between the first reflection zeros around the maximum reflectivity. At first sight, one may erroneously deduce from (2.76a) and (2.81a) that such pair of reflection zeros are obtained by forcing $\gamma = 0$. However, notice that by applying the l'Hôpital's rule, S_{11} and S_{22} tend to a finite value in the limit when $\gamma \to 0$. Indeed, the frequency corresponding to the first minimum of reflection satisfies

$$\gamma L = j\pi \tag{2.87}$$

or

$$|k|^2 + \frac{\pi^2}{L^2} = (\Delta\beta)^2 \tag{2.88}$$

and assuming that ε_{re} does not depend on frequency in the rejected bandwidth (i.e., neglecting dispersion), the bandwidth is found to be

$$\mathrm{BW} = \frac{c|k|}{\pi\sqrt{\varepsilon_{\mathrm{re}}}}\sqrt{1+\left(\frac{\pi}{|k|L}\right)^2} \tag{2.89}$$

2.4.5 Relation between the Coupling Coefficient and the S-Parameters

As discussed in Section 2.4.3, as long as the coefficients of the Fourier series expansion of the coupling coefficient, K_n, are different than zero, stop bands in the vicinity of those frequencies satisfying the phase matching condition (2.63) are expected in EBG-based periodic transmission lines. In other words, the number of reflection bands is intimately related to the harmonic content of the coupling coefficient $K(z)$. For instance, it is expected that for a sinusoidal coupling coefficient, a single reflection band, centered at the frequency given by (2.84) with $n = 1$, appears. Indeed, under conditions of low reflectivity, the relation between S_{11} and $K(z)$ can be easily approximated by the Fourier transform. To demonstrate this, let us express the generalized reflection coefficient in an EBG structure as

$$\rho(z) = \frac{a^-(z)}{a^+(z)} \tag{2.90}$$

and let us consider the coupled mode equations (2.47a and 2.47b), where the only approximation applied is single-mode operation. Using (2.47), the derivative of ρ with z can be expressed as [14]:

$$\frac{d\rho(z)}{dz} = 2j\cdot\beta\cdot\rho(z) + K(z)\left(1-\rho(z)^2\right) \tag{2.91}$$

which is a nonlinear equation that does not have a known general solution. However, if it is assumed that β is not a function of z, and $|\rho\ (z)|^2 << 1$ (low reflectivity conditions), (2.91) can be expressed as [23]

$$\frac{d\rho(z)}{dz}\cdot e^{-2j\beta z} = 2j\cdot\beta\cdot\rho(z)\cdot e^{-2j\beta z} + K(z)\cdot e^{-2j\beta z} \tag{2.92}$$

where the equation has been multiplied by $e^{-2j\beta z}$. The previous equation can be simplified to

$$\frac{d}{dz}\left(\rho(z)\cdot e^{-2j\beta z}\right) = K(z)\cdot e^{-2j\beta z} \tag{2.93}$$

and integrating both sides between $z = 0$ and $z = L$, the following result is obtained:

$$\rho(L)\cdot e^{-2j\beta L}-\rho(0)=\int_0^L K(z)\cdot e^{-2j\beta z}\cdot dz \tag{2.94}$$

If we now assume that the output port is matched, then $\rho(L)=0$, and $\rho(0)\equiv S_{11}$. Therefore,

$$S_{11}=-\int_0^L K(z)\cdot e^{-2j\beta z}\cdot dz \tag{2.95}$$

and (2.95) resembles the Fourier transform of $K(z)$. If we assume that $K(z)=0$ for $z<0$ and for $z>L$ (device with length L, between $z=0$ and $z=L$), (2.95) can be rewritten as follows:

$$S_{11}=-\int_{-\infty}^{\infty} K(z)\cdot e^{-j2\pi\left(\frac{\beta}{\pi}\right)z}\cdot dz \tag{2.96}$$

and (2.96) is the Fourier transform of $K(z)$ in the variable β/π, that is,

$$S_{11}\left(\frac{\beta}{\pi}\right)=-\mathbf{F}(K(z)) \tag{2.97}$$

Although $K(z)$ is zero outside the interval $[0,L]$, in a first-order approximation we can introduce the series expansion (2.58) of $K(z)$ in (2.96). According to this, the reflection coefficient S_{11} will be significant in the vicinity of those frequencies satisfying

$$\frac{n}{l}=\frac{\beta}{\pi} \tag{2.98}$$

which is identical to the phase matching condition (2.63). Thus, in summary, the harmonic content of the coupling coefficient determines the frequency behavior of the reflection coefficient, and gives the number of rejected bands. This is a fundamental property that can be helpful in certain applications. However, the exact determination of S_{11} from (2.97) in situations where high reflectivity is required (as occurs in most practical applications) is not possible.

2.4.6 Using the Approximate Solutions of the Coupled Mode Equations

The aim of this subsection is to provide two examples to illustrate the use of the approximate analytical solutions of the coupled mode equations and to compare the results with full-wave EM simulations and measurements of the considered structures (further results are given in Ref. [22]). Let us first consider a periodic microstrip

transmission line with a coupling coefficient $K(z)$ exhibiting a sinusoidal dependence on z. A rejection band in the vicinity of that frequency satisfying the phase matching condition (i.e., 2.63 with $n = 1$) is expected. However, according to the preceding theory, since $K(z)$ does not have harmonic content, further rejection bands will not appear. In order to determine the variation of the characteristic impedance with the axial position, let us integrate (2.50) with z (the dependence on ω is considered to be negligible). This gives

$$-2\int_0^z K(z')\cdot dz' = \int_{Z_o(0)}^{Z_o(z)} \frac{1}{Z_o'}\cdot dZ_o' \tag{2.99}$$

where integration is performed between $z = 0$ and an arbitrary point, z, within the periodic microstrip line. Solution of (2.99) gives

$$Z_o(z) = Z_o(0)\cdot e^{-2\int_0^z K(z')\cdot dz'} \tag{2.100}$$

Let us now assume that the periodic structure exhibits a continuous variation of the characteristic impedance at the extremes of the device ($z = 0$ and $z = L$)—the characteristic impedance at these extremes being $Z_o(0) = Z_o(L) = Z_{o,ref}$, that is, the reference impedance of the ports and access lines. Moreover, let us consider that the impedance in the periodic region (interval $[0,L]$) experiences variations around $Z_{o,ref}$ and starts increasing from the input port. This forces the coupling coefficient to be expressed as

$$K(z) = -2|K_1|\cdot\cos\left(\frac{2\pi}{l}z\right) = 2|K_1|\cdot\cos\left(\frac{2\pi}{l}z + \pi\right) \tag{2.101}$$

where K_1 is the first term of the Fourier series expansion of $K(z)$ and $\arg(K_1) = \pi$ (the other terms are null). Introducing (2.101) in (2.100), the characteristic impedance is found to be

$$Z_o(z) = Z_{o,ref}\cdot e^{\frac{2|K_1|l}{\pi}\sin\left(\frac{2\pi}{l}z\right)} \tag{2.102}$$

For the present example, the period of the EBG structure and the reference impedance of the ports are set to $l = 1$ cm and $Z_{o,ref} = 50\ \Omega$, respectively, and 10 unit cells are considered, that is, $L = 10l = 10$ cm. In order to avoid extreme characteristic impedances along the line, the coupling coefficient amplitude is set to $|K_1| = 0.64\ \text{cm}^{-1}$. This gives maximum and minimum characteristic impedances of $Z_{o,max} = 1.50Z_{o,ref} = 75\ \Omega$ and $Z_{o,min} = 0.66Z_{o,ref} = 33.3\ \Omega$, respectively. The considered substrate parameters are those of the *Rogers RO3010* substrate, with thickness $h = 1.27$ mm and dielectric constant $\varepsilon_r = 10.2$. In the present example, the periodic perturbation of the characteristic impedance of the line is carried out by varying the strip width,

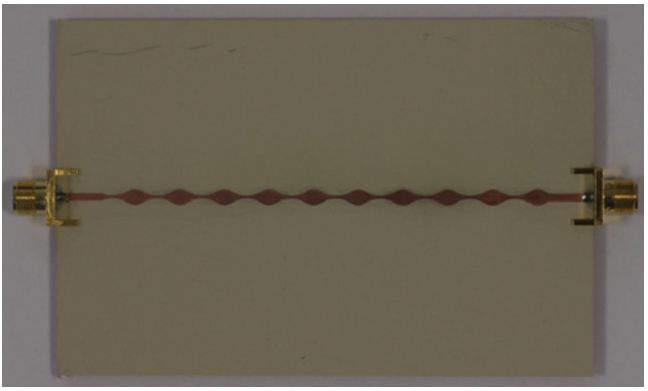

FIGURE 2.10 Photograph of the EBG microstrip line with sinusoidal coupling coefficient.

W, along the line.[30] In practice, the width of the line as a function of the characteristic impedance can be obtained by means of a transmission line calculator. A simple procedure is to calculate the line width at discrete points along the period, and then approximate $W(z)$ by a piecewise function. The photograph of the resulting microstrip EBG structure, including access lines, is depicted in Figure 2.10. The reflection (S_{11}) and transmission (S_{21}) coefficients of the structure inferred from full-wave EM simulation and measurement are compared with those given by expressions (2.76) in Figure 2.11. The analytical solutions (2.76) have been obtained by considering $n = 1$, $k = -jK_1 = j0.64\ \text{cm}^{-1}$, $l = 1$ cm, and β given by

$$\beta = \frac{2\pi f}{c}\sqrt{\varepsilon_{\text{re}}} \tag{2.103}$$

with ε_{re} inferred from (2.57). The agreement between the predictions of analytical solutions of the coupled mode theory and the full-wave simulation and experimental results is remarkable. The frequency of maximum attenuation, the value of maximum reflectivity, the value of minimum transmission, and the bandwidth, obtained from expressions (2.84–2.86), and (2.89), respectively, are found to be $f_{\max} = 5.66$ GHz, $|S_{11}|_{\max} \sim 1$ (i.e., ~0 dB), $|S_{21}|_{\min} = 3.32 \times 10^{-3}$ (i.e., −49.6 dB) and BW = 2.55 GHz. As expected, these values are in good agreement with those inferred from the frequency response depicted in Figure 2.11.

It is clear in view of Figure 2.11 that the frequency response of the designed microstrip EBG structure exhibits a single reflection band around $f_{\max}$. No further forbidden bands are present, as one expects from the lack of harmonic content of the considered coupling coefficient, $K(z)$. Conversely, by considering a coupling coefficient given by a square-shaped periodic function of the form indicated in Figure 2.12, forbidden bands centered at the fundamental frequency and its odd-order harmonics are expected, as derived from the harmonic content of such coupling coefficient. From

[30] The characteristic impedance in microstrip transmission lines can also be modulated through ground plane etching, as will be later shown.

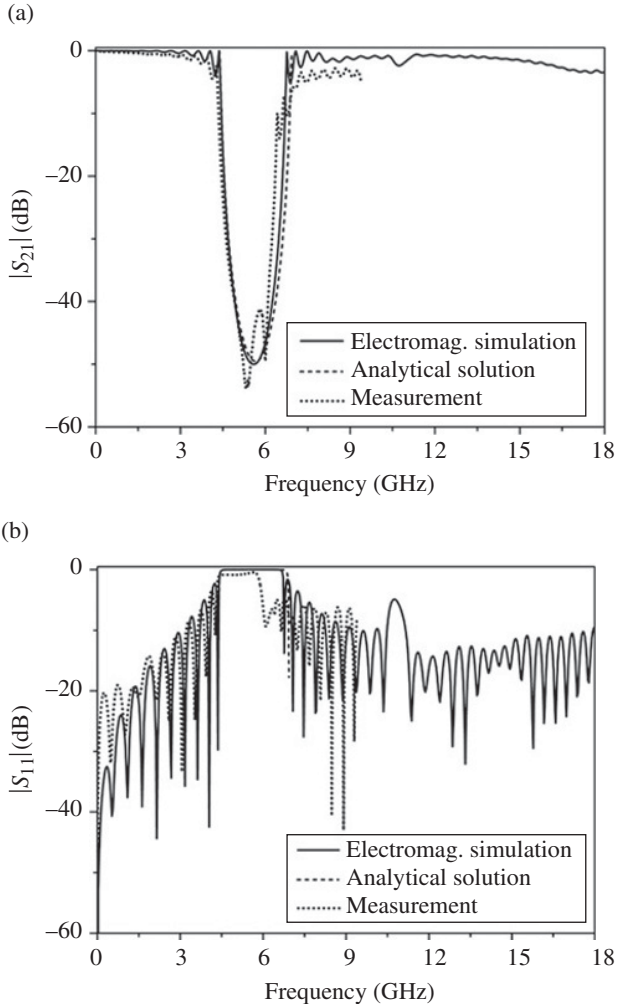

FIGURE 2.11 Frequency response of the EBG structure depicted in Figure 2.10. (a) Insertion loss and (b) return loss. The measurement is depicted up to 10 GHz. The EM simulations have been obtained by excluding ohmic and dielectric losses.

(2.100), the characteristic impedance corresponding to the coupling coefficient of Figure 2.12 can be expressed as a piecewise function in one period, l, as follows:

$$Z_o(z) = Z_{o,ref} \cdot e^{2Kz}, \qquad z \in \left[0, \frac{l}{4}\right] \tag{2.104a}$$

$$Z_o(z) = Z_{o,ref} \cdot e^{-2K\left(z-\frac{l}{2}\right)}, \quad z \in \left[\frac{l}{4}, \frac{3l}{4}\right] \tag{2.104b}$$

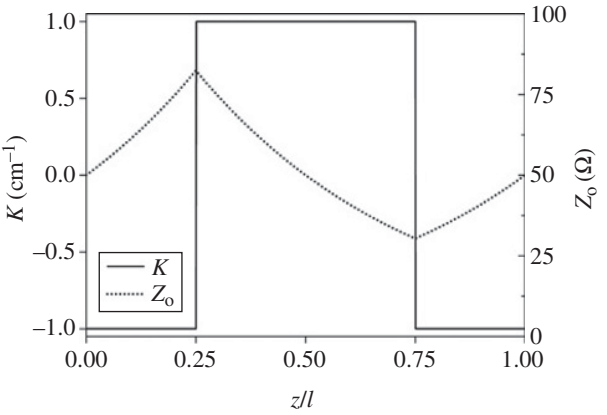

FIGURE 2.12 Dependence of the coupling coefficient and characteristic impedance with the axial position z, corresponding to an EBG microstrip line with a square shaped coupling coefficient.

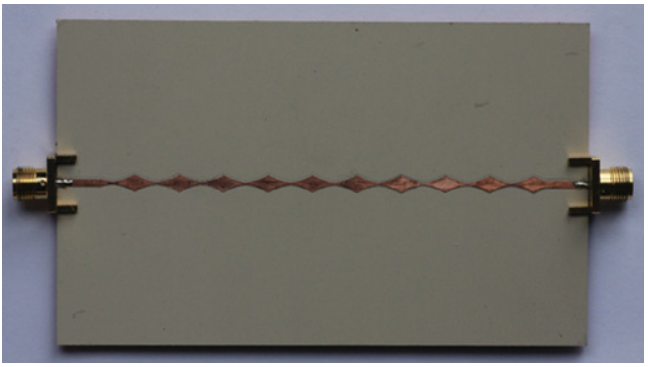

FIGURE 2.13 Photograph of the EBG microstrip line with square-shaped coupling coefficient.

$$Z_o(z) = Z_{o,ref} \cdot e^{2K(z-l)}, \qquad z \in \left[\frac{3l}{4}, l\right] \tag{2.104c}$$

where K is the amplitude of the coupling coefficient (the characteristic impedance is also depicted in Fig. 2.12). The 10-cell microstrip EBG structure shown in Figure 2.13 exhibits a dependence of the characteristic impedance with the axial position given by (2.104), with $l = 1$ cm and $K = 1$ cm^{-1}. With these parameter values, the characteristic impedance varies around the reference impedance with extreme values given by $Z_o(l/4) = Z_{o,max} = 1.65Z_{o,ref} = 82.4\ \Omega$, and by $Z_o(3l/4) = Z_{o,min} = 0.61Z_{o,ref} = 30.4\ \Omega$

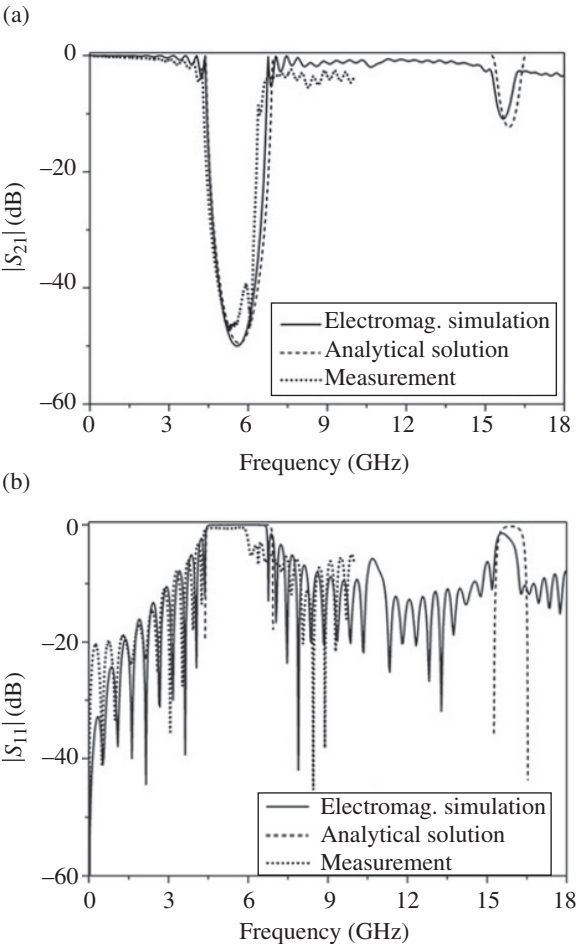

FIGURE 2.14 Frequency response of the EBG structure depicted in Figure 2.13. (a) Insertion loss and (b) return loss. The measurement is depicted up to 10 GHz. The EM simulations have been obtained by excluding ohmic and dielectric losses.

(the considered substrate is also the *Rogers RO3010* with thickness $h = 1.27$ mm and dielectric constant $\varepsilon_r = 10.2$). The broadband frequency response of the designed microstrip EBG structure, depicted in Figure 2.14, confirms that only the fundamental and odd harmonics are reflected, and the frequencies of maximum attenuation are given by (2.84) with n odd. The value of minimum transmission in each forbidden band can be obtained from (2.86), with k given by (2.66), where the terms of the coupling coefficient are given by

$$K_n = -\frac{2K}{n\pi}, \quad n = 1,3,5,\ldots \tag{2.105}$$

Thus, the minimum transmission at the first three forbidden bands, inferred from analytical expressions, is −49.3 dB, −12.5 dB, and −5.7 dB; these values are in good agreement with the frequency response of the device, confirming the validity of the theory.

2.5 APPLICATIONS

Several applications of periodic transmission lines, including nonuniform transmission lines and reactively loaded lines, are reviewed in this section.

2.5.1 Applications of Periodic Nonuniform Transmission Lines[31]

As it has been demonstrated along this chapter, periodic transmission lines with conductor strip or ground plane modulation exhibit stop bands and pass bands that can be useful in various applications. These applications include reflectors, high-Q resonators, spurious suppression in planar microwave filters, and harmonic suppression in active circuits, among others. In the next subsections, such applications are discussed and some examples are reported. Moreover, it will be shown that quasi-periodic nonuniform transmission lines are useful to implement chirped delay lines (CDLs).

2.5.1.1 Reflectors Band gap structures were first applied to the optical domain as photonic bandgaps (PBGs) [24], and later used for the implementation of reflectors at microwave frequencies in microstrip technology [18, 25]. The first EBG structures in microstrip technology were indeed implemented by drilling a two-dimensional periodic pattern of holes through the substrate [25, 26]. A simpler strategy to inhibit signal propagation at controllable frequencies consists of partially etching the ground plane as depicted in Figure 2.15 [18]. As reported in Ref. [18], this structure exhibits wider and deeper stopbands than previous designs using the dielectric hole approach [25]. However, the effects of the perturbation are negligible beyond the defect row below the conductor strip [19]. This suggests that EBG reflectors consisting of only the central row of the pattern (one-dimensional EBG) will have similar behavior as a two-dimensional reflector, with the advantage of a considerable reduction in the transverse dimension. Figure 2.16a depicts a one-dimensional and a two-dimensional reflector with a period of $l = 18.9$ mm, giving a Bragg frequency of 3 GHz in the considered substrate (the *Rogers RO3010*, with dielectric constant $\varepsilon_r = 10.2$ and thickness $h = 1.27$ mm). The ratio between the radius of the circles and the period is 0.25. Figure 2.16b indicates that the frequency responses of both structures are almost undistinguishable. Hence, the one-dimensional EBG transmission line suffices to achieve strong reflection at the operating frequency.

[31] This subsection has been co-authored with Txema Lopetegi (Public University of Navarre, Spain).

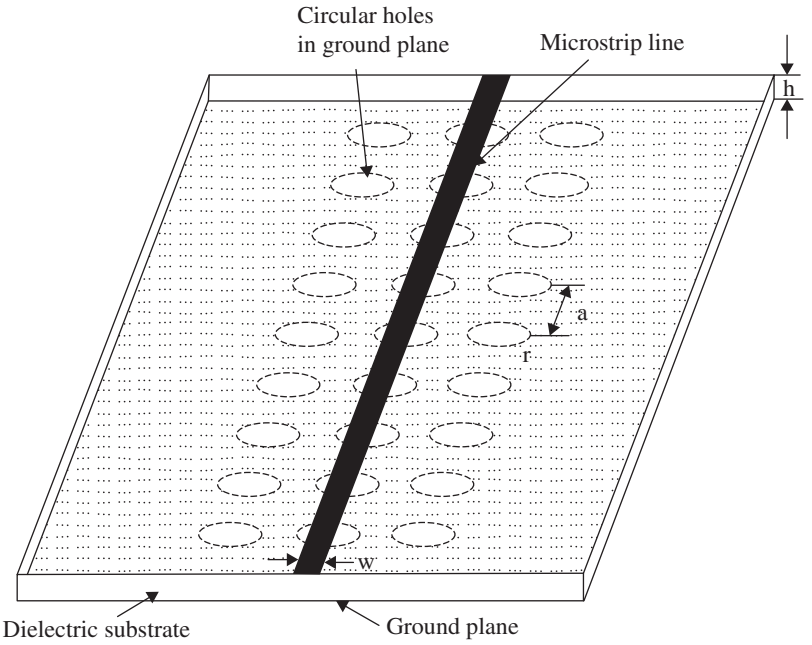

FIGURE 2.15 Microstrip EBG structure implemented by etching circular holes in the ground plane. Reprinted with permission from Ref. [18]; copyright 1998 IEEE.

In order to reduce the ripple in the pass bands, inherent to periodic structures, a tapering technique, consisting of a modification of the radius of each circle according to the position in the structure, can be applied [27]. The improvement of the frequency response achieved by means of the tapering function is related to the progressive matching of the characteristic impedance of the Bloch wave toward the input and output characteristic impedance that the tapering function produces. It is also possible to enhance the bandwidth of EBG microstrip lines by using chirping techniques, formerly used in fiber Bragg gratings [28]. The idea is to linearly distribute the position of the etched holes (center-to-center distance of adjacent holes) along the line [29]. This modulation of the period has the effect of varying the Bragg frequency along the line, with the result of an enhanced bandwidth. The effects of tapering and chirping can be appreciated in Figure 2.17, where the frequency responses of a nonchirped, chirped, and tapered and chirped EBG microstrip lines are compared. Chirping the lines clearly enhances the rejected bandwidth, whereas the pass band ripple level is significantly reduced by tapering the structure.

If a strong rejection level and sharp cutoff is required, the number of periods of the structure has to be necessarily large. To avoid an excessive aspect ratio (length versus width) of the one-dimensional EBG microstrip line, it is possible to bend the line as depicted in Figure 2.18 [30]. The tapering and chirping techniques can be applied to these bended EBG structures as well, in order to enhance the reflection bandwidth and reduce the ripple level in the pass bands [14].

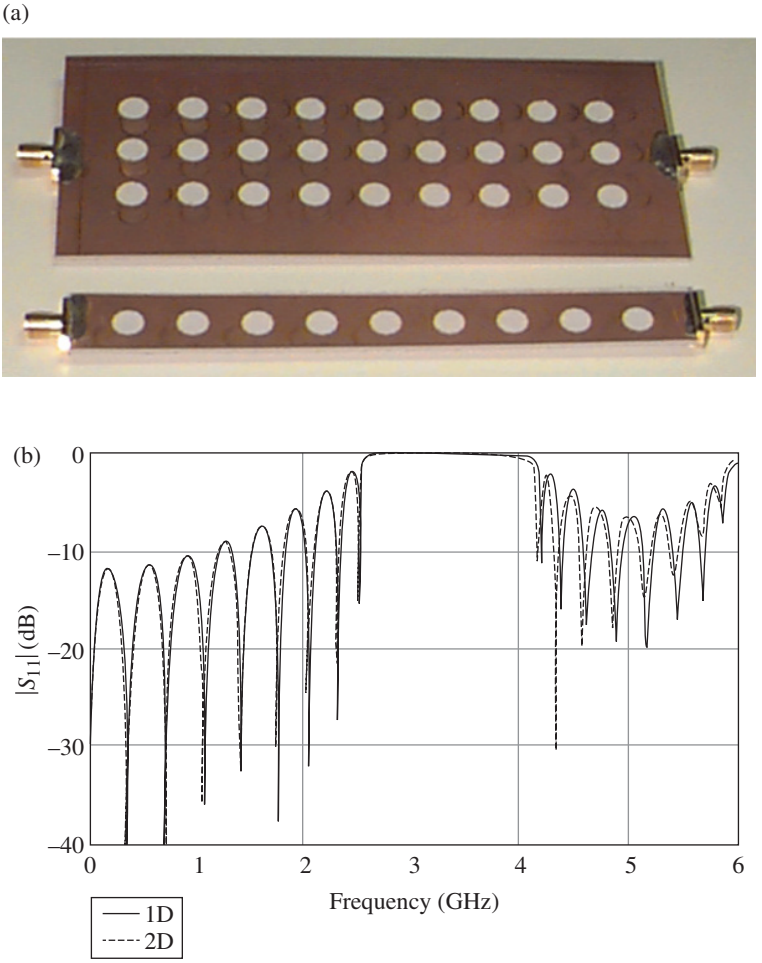

FIGURE 2.16 Two-dimensional and one-dimensional EBG microstrip line (a) and measured reflection coefficient (b). The line width is $W = 1.2$ mm corresponding to a 50 Ω line in the considered substrate. Reprinted with permission from [19]; copyright 1999 John Wiley.

It was shown in Section 2.4.5 that the harmonic content of the coupling coefficient $K(z)$ determines the number of rejected bands in the frequency response of EBG-based transmission lines, and this was verified in Section 2.4.6 by considering two different periodic structures. Specifically, it was demonstrated that a square-shaped coupling coefficient produces stop bands not only at the fundamental frequency but also at its odd harmonics. However, the rejection level decreases with the frequency index; and for certain applications, it may be of interest to achieve two, or even further, rejected bands centered at frequencies not necessarily being harmonics. To implement multiple-frequency-tuned EBG transmission lines, a solution is to add various sinusoidal functions tuned at the design frequencies, as reported in Ref. [31]. Specifically,

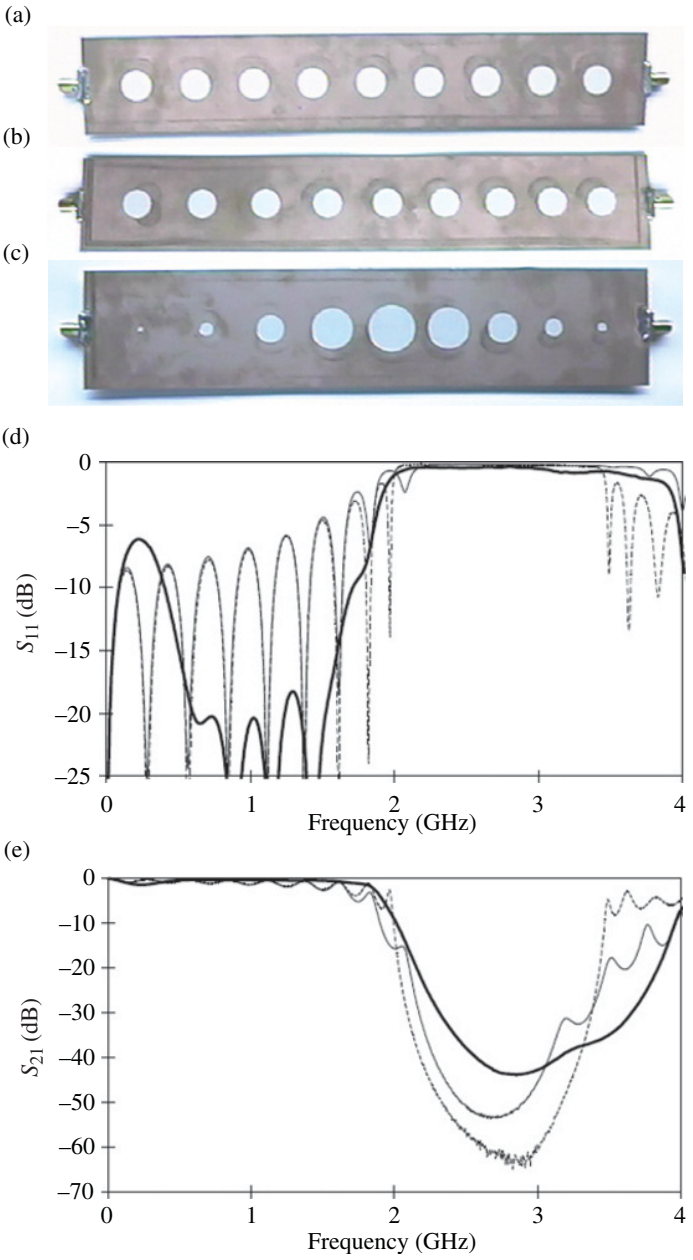

FIGURE 2.17 Photographs of a nonchirped (a), chirped (b), and tapered and chirped (c) EBG microstrip lines, measured return loss (d) and measured insertion loss (e). The traces are dashed line (nonchirped), thin solid line (chirped), and thick solid line (tapered and chirped). Reprinted with permission from Ref. [29]; copyright 2000 John Wiley.

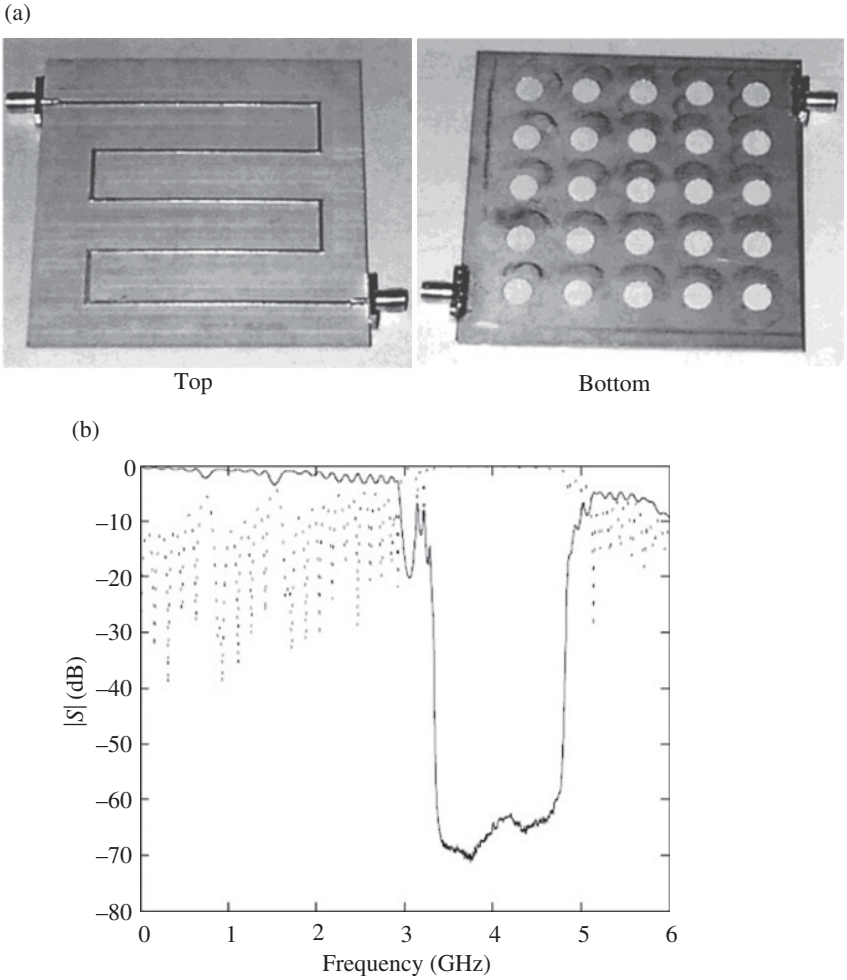

FIGURE 2.18 Photograph of a bended EBG microstrip line (a) and measured insertion (solid line) and return (dashed line) loss (b). The substrate is the *Rogers RO3010* with dielectric constant $\varepsilon_r = 10.2$ and thickness $h = 1.27$ mm. The period of the structure is $l = 15.5$ mm, the ratio between the radius and the period is 0.25 and the strip width is 1.2 mm (corresponding to a 50 Ω line). Reprinted with permission from Ref. [30]; copyright 1999 John Wiley.

the double- and triple-frequency-tuned EBG structures of Ref. [31] are implemented by adding two and three raised-sine functions, respectively. The double-tuned EBG has 9 periods of $l_1 = 23.9$mm and 14 periods of $l_2 = 14.8$ mm, in order to have the rejected frequencies around 3 GHz and 4.5 GHz, respectively. Both sine functions have an amplitude-to-period ratio of $t/l = 0.2$. The triple-frequency-tuned EBG microstrip structure is designed with three added raised-sine functions. The first sine has 9 periods of $l_1 = 23.9$ mm, the second one has 11 periods of $l_2 = 19.35$ mm, and the third one has 14 periods of $l_3 = 14.8$ mm, to obtain their stop bands centered at 3 GHz, 4 GHz,

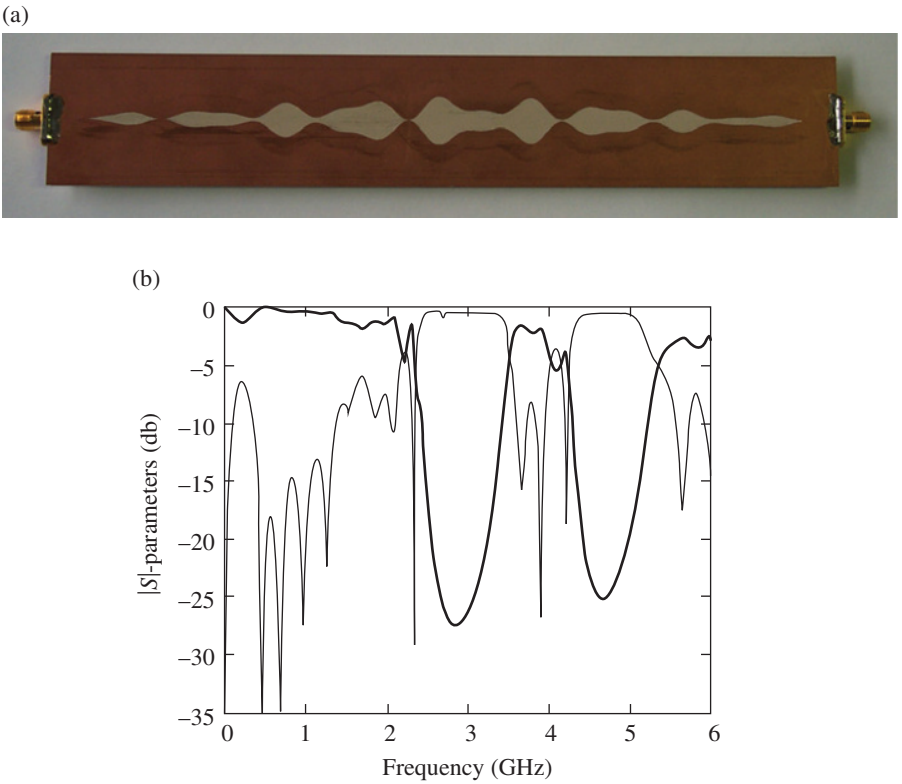

FIGURE 2.19 Photograph (ground plane) of a double-frequency-tuned EBG microstrip line (a) and measured insertion (thick line) and return (thin line) loss (b). The substrate is the *Rogers RO3010* with dielectric constant $\varepsilon_r = 10.2$ and thickness $h = 1.27$ mm. The conductor strip width is $W = 1.2$ mm. Reprinted with permission from Ref. [31]; copyright 2000 IEEE.

and 5 GHz, respectively. In all these cases, the t/l ratio is fixed to 0.15. The amplitude of each particular sine is limited in order to maintain the total amplitude of the ground plane perturbation in such values that radiation is kept in low levels. In both designs, the patterns resulting from the addition of various sine functions are Hamming-windowed to achieve a low-rippled response at the pass band [31]. These double- and triple-tuned EBG microstrip lines, including their frequency responses, are depicted in Figures 2.19 and 2.20, respectively.[32] The results of these figures clearly demonstrate that band gaps at closely spaced frequencies can be achieved. Notice that the patterned functions in the ground plane do not give a combination of pure sinusoidal functions for the coupling coefficient, and, hence, further stops bands at the harmonics of the design frequencies may appear.

[32] The raised sine functions determine the geometry of the slotted ground plane, rather than the coupling coefficient. Nevertheless, for small perturbations, the harmonic content of the rejected bands can be approximated by the Fourier transform of the perturbation geometry.

(a)

(b)

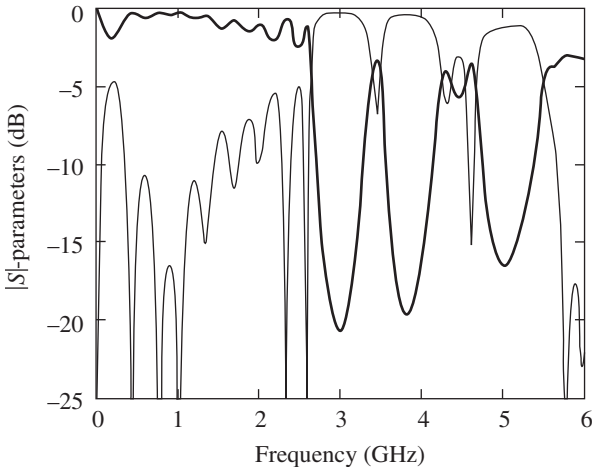

FIGURE 2.20 Photograph (ground plane) of a triple-frequency-tuned EBG microstrip line (a) and measured insertion (thick line) and return (thin line) loss (b). The substrate is the *Rogers RO3010* with dielectric constant $\varepsilon_r = 10.2$ and thickness $h = 1.27$ mm. The conductor strip width is $W = 1.2$ mm. Reprinted with permission from Ref. [31]; copyright 2000 IEEE.

2.5.1.2 High-Q Resonators It is possible to implement Bragg resonators by combining two EBG-based reflectors separated by a microstrip line acting as a resonant cavity [32]. In principle, such resonant cavity can be obtained by removing one cell of the EBG structure, which corresponds to a resonator structure with two uniform EBG reflectors separated by a 180° line at the Bragg frequency of the reflector. However, since the reflectors contribute to the phase, the resonance condition is written as [33] follows:

$$\phi_{\text{ref1}}(f_o) + \phi_{\text{ref2}}(f_o) - 2\cdot\beta(f_o)\cdot L_m = 2\pi n \tag{2.106}$$

where n is an integer that must be chosen so that the resonance frequency lies within the reflected frequency band of the EBG reflectors. The other variables of (2.106) are as follows:

- ϕ_{ref1}: phase of the reflection coefficient of the first reflector
- ϕ_{ref2}: phase of the reflection coefficient of the second reflector
- β: phase constant of the mode of interest in the resonant cavity
- L_m: length of the microstrip transmission line that separates the two reflectors

Thus, the length of the resonant cavity must be optimized in order to satisfy (2.106) at the required frequency. To this end, it is necessary to study the reflectors independently and obtain the phase of the reflection coefficient at the design frequency, that is, ϕ_{ref1} and ϕ_{ref2}. Once these phases are known (they are identical if the same reflectors are considered at both sides of the resonant cavity), the electrical length of the line can be inferred, and from the value of the phase constant, the length L_m can be determined. Figure 2.21a shows the photograph of the fabricated Bragg reflector reported in Ref. [32], where $\phi_{ref1} = \phi_{ref2} = -95.84^\circ$ at the design frequency ($f_o = 4.2$ GHz), which gives $\beta L_m = 84.15^\circ$ for $n = -1$ and $L_m = 6.25$ mm. The considered substrate is the *Rogers RO3010* with dielectric constant $\varepsilon_r = 10.2$, thickness $h = 1.27$ mm, and $\tan\delta = 0.0026$. Hole dimensions and separations are those of Figure 2.16. The measured frequency response of this resonator is depicted in Figure 2.21b, where the resonance is located at the desired frequency, and the measured quality factor is $Q = 129.2$, as reported in Ref. [32], which is a high value for a planar structure. Other high-Q resonators based on a similar concept but implemented in CPW, CPS and slot lines are reported in Ref. [34].

2.5.1.3 Spurious Suppression in Planar Filters One of the most interesting applications of EBG-based transmission lines acting as Bragg reflectors is the suppression of undesired harmonics in planar microwave filters. Indeed, in the EBG-based reflectors discussed before, the periodic perturbation was achieved through ground plane etching. However, it is also possible to modulate the strip width leaving the ground plane unaltered, as was pointed out in Section 2.4.6. This eases fabrication, and it is an interesting solution in those applications where the structure must rest on top of a metallic holder. This latter approach was applied to the design of coupled line microstrip bandpass filters with spurious suppression [35]. In such filters, the width of the coupled lines was perturbed following a sinusoidal law. This modulates the characteristic impedance so that the harmonic pass band of the filter is rejected (first spurious band), while the desired pass band is maintained virtually unaltered. In this "wiggly-line" filter, the period of the perturbation, l, is obtained following:

$$l = \frac{\lambda_g}{4} \tag{2.107}$$

where λ_g is the guided wavelength at the design frequency (filter central frequency). According to expression (2.107), it is clear that in each coupled line section exactly a complete period of the perturbation can be accommodated. The perturbation has been implemented in Ref. [35] through the modulation of the outer edge of the coupled

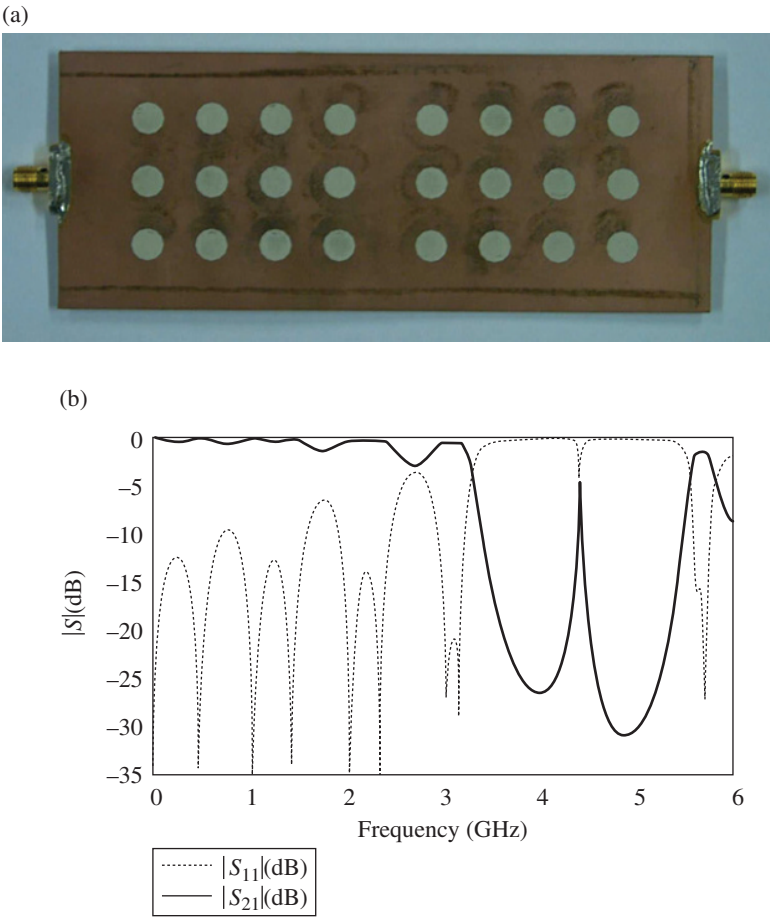

FIGURE 2.21 Photograph (ground plane) of the Bragg resonator (a) and measured frequency response (b). The conductor strip width is $W = 1.2$ mm. Reprinted with permission from Ref. [32]; copyright 1999 Springer.

lines (i.e., leaving the inner edge unaltered). The conductor strip-width variation in each coupled line section (denoted by the index i) is given by

$$W_i(z) = W_i\left(1 + \frac{M(\%)}{100}\cos\left(\frac{2\pi z}{l_i} + \phi\right)\right) \tag{2.108}$$

where W_i is the width of the coupled lines in the conventional implementation, ϕ is the initial phase (0° or 180°), l_i is the period of the sinusoidal perturbation, and M is the strip width modulation parameter.

A prototype device of a "wiggly line" coupled line bandpass filter is depicted in Figure 2.22 [35]. It is an order-3 Butterworth bandpass filter centered at 2.5 GHz with a 10% fractional bandwidth and a strip width perturbation factor $M = 47.5\%$. This filter was implemented on the *Rogers RO3010* substrate with $\varepsilon_r = 10.2$ and $h = 1.27$ mm. The measured frequency response of this device is also depicted in Figure 2.22 jointly with that frequency response which was obtained on an identical filter, but with different modulation factor (i.e., $M = 37.5\%$). The results indicate that in both cases, the pass band of interest is not affected by the strip width modulation, whereas significant rejection of the first spurious band is achieved. This is over 40 dB in the "wiggly line" filter with $M = 47.5\%$.

It has also been implemented a microstrip coupled line bandpass filter with multispurious suppression [36]. To this end, the modulation of the widths of the coupled line sections was done by means of different periods, so that very good out-of-band performance was demonstrated, with spurious suppression above 30 dB up to the fourth harmonic. The device and the measured frequency response are depicted in Figure 2.23 (further details are given in Ref. [36]).

2.5.1.4 Harmonic Suppression in Active Circuits Harmonic suppression in active circuits, such as power amplifiers, mixers, oscillators, or active antennas, using EBGs is very interesting in order to improve device performance. By reducing the harmonic content, the power level at the fundamental frequency increases, and the efficiency of the device can be enhanced [37–40]. It has also been demonstrated that EBG structures are useful to reduce the phase noise in microwave oscillators [41]. In this case, the key idea is to increase the quality factor of the resonator by effectively increasing the phase slope of the input matching network through the stopband effect of the periodic structure.

In Refs. [37–39], the EBG structures are cascaded to the output of the devices, whereas in Refs. [40, 41] the periodic structure is integrated with the active device. This latter strategy was also used for the design of an active antenna with improved efficiency, where a multiple-tuned EBG structure was used in order to achieve the suppression of the even and the odd harmonics [14]. The design of EBG-based active circuits is a two-step process: first, the conventional (i.e., without EBG) device is designed according to the procedures described in well-known textbooks [10]; second, the EBG, which is independently designed, is introduced in the active device in order to suppress the harmonic content. The active circuit design (first step) is out of the scope of this book. Therefore, let us review the design of the active antenna reported in Ref. [14], with emphasis on the design of the EBG, as an illustrative example of the potentiality of periodic structures to improve the performance of active circuits.

The active antenna consists of a microwave oscillator directly feeding a patch antenna. The introduction of the EBG within the oscillator circuit has the effect of suppressing the harmonics present in the radiated power spectrum, increasing at the same time the power level at the fundamental frequency. One important aspect of the active antenna reported in Ref. [14] is the use of a double-tuned EBG, which effectively reduces the power level of the first ($2f_o$) and second ($3f_o$) harmonic

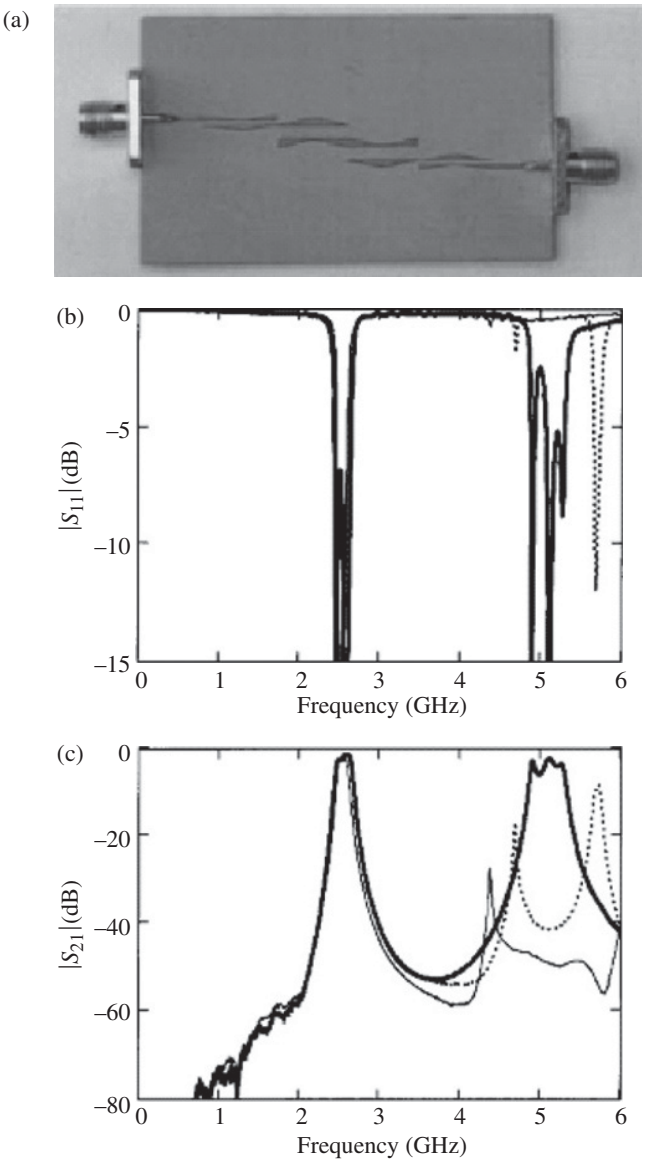

FIGURE 2.22 Coupled line bandpass filter with strip width modulation (a) and measured return (b) and insertion (c) loss. Conventional: thick solid line; "wiggly line" filter with $M = 37.5\%$: dashed line; "wiggly line" filter with $M = 47.5\%$: thin solid line. Reprinted with permission from Ref. [35], copyright 2001 IEEE.

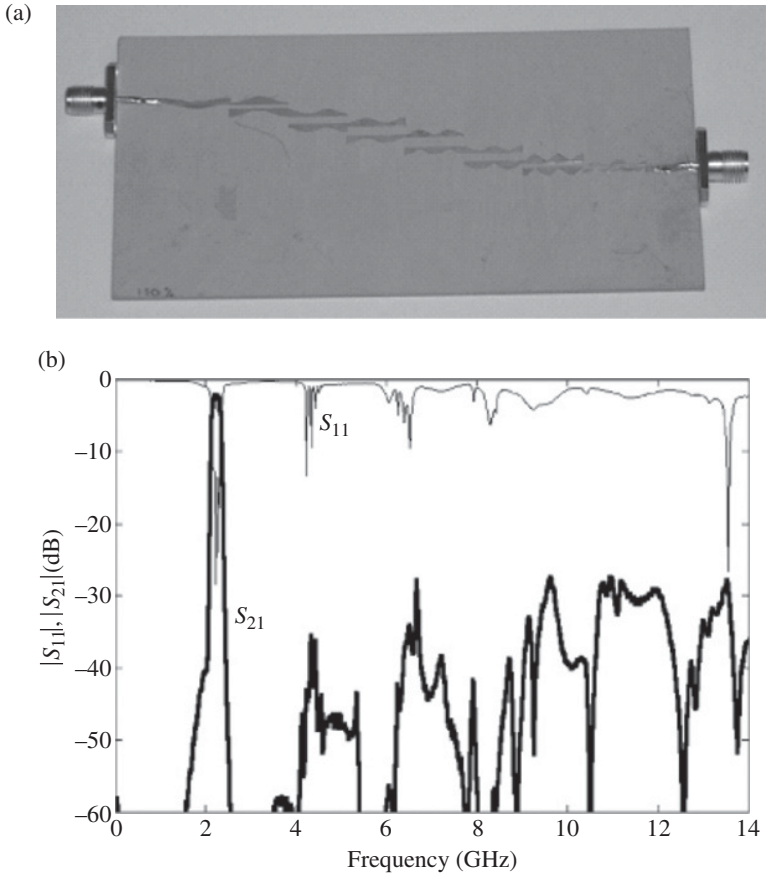

FIGURE 2.23 Coupled line bandpass filter with multispurious rejection (a) and measured frequency response (b). Reprinted with permission from Ref. [36], copyright 2004 IEEE.

(notice that by using a single tuned EBG structure at $2f_o$, the odd-order harmonics, i.e., $3f_o$, $5f_o$, etc., cannot be suppressed). Specifically, the considered EBG is formed by the addition of two raised sinusoids etched in the ground plane, and tuned at $2f_o$ and $3f_o$. The photograph of the classical designed active antenna of Ref. [14] is depicted in Figure 2.24a, where the patch antenna is the terminating load of the oscillator. The considered transistor is the Si bipolar junction transistor (BJT) *AT-42035*, operating in the common-base configuration at $V_{CE} = 8$ V and $I_C = 35$ mA. The oscillation frequency was set to $f_o = 4.5$ GHz, which means that the EBG structure must be able to efficiently suppress those frequencies in the vicinity of 9 GHz and 13.5 GHz. The periods of the raised sinusoids are 6.2 mm (to reject the first harmonic) and 4.1 mm (to reject the second harmonic), whereas the amplitude of the perturbation to period ratio is 0.3 for both raised sinusoids (the *Rogers RO3010* substrate with thickness $h = 1.27$ mm and dielectric constant $\varepsilon_r = 10.2$ was used). Figure 2.24b shows the

(a)

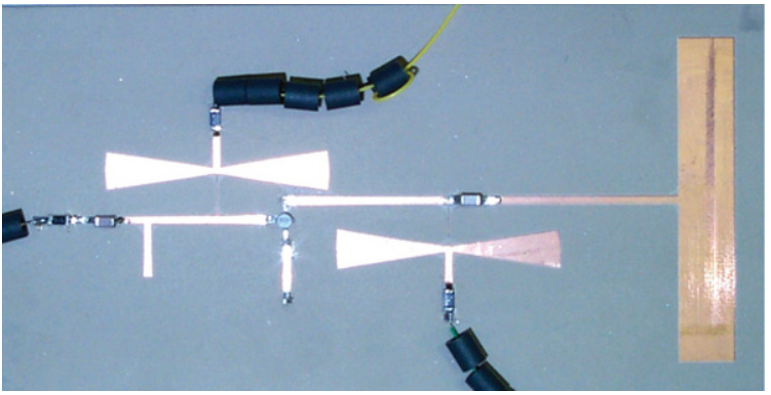

(b)

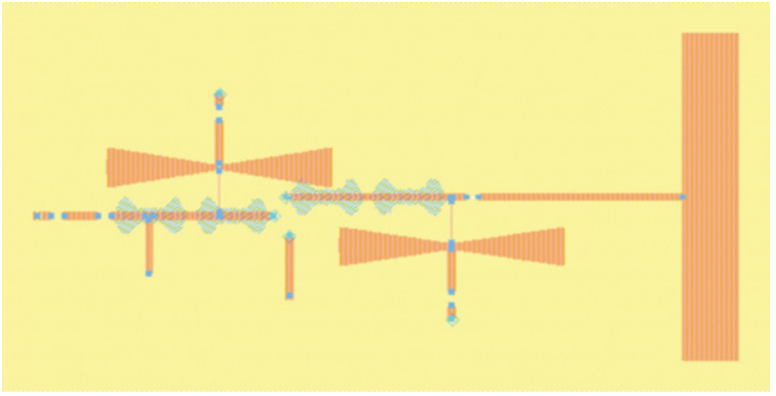

FIGURE 2.24 Photograph of the classical active antenna designed in Ref [14] (a) and layout of the same antenna including the EBG structure to reject the first and second harmonics (b). From Ref. [14]; reprinted with permission from the author.

layout of the active antenna, including the double-tuned EBG, etched in the ground plane, and integrated within the oscillator matching networks. The measured power spectrum of both antennas (with and without EBG), inferred by means of a spectrum analyzer and a rectangular horn antenna optimized for the fundamental oscillation, is depicted in Figure 2.25. For the prototype with EBG, the first and second harmonic are reduced around 20 dB and 10 dB, respectively, whilst an increase of the output power of roughly 2.6 dB at the fundamental frequency is achieved. It is important to highlight that the introduction of the EBG structure within the oscillator circuit did not require a redesign process. Moreover, this approach does not increase the layout area.

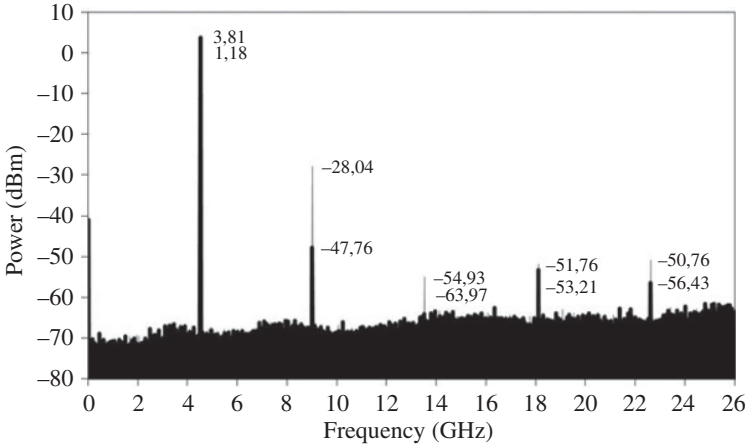

FIGURE 2.25 Measured power spectrum for the classical active antenna (thin line) and for the active antenna with EBG (thick line). From Ref. [14]; reprinted with permission from the author.

2.5.1.5 Chirped Delay Lines A CDL is a quadratic-phase filter whose frequency response $H(\omega) = A_0(\omega) \cdot \exp(-j \cdot \phi_0(\omega))$ is characterized by constant insertion losses, $A_0(\omega)$, and a group-delay, $\dot{\phi}_0 = d\phi_0/d\omega$, that varies linearly with frequency in the operation bandwidth. CDLs are extensively used in the emerging field of microwave analog signal processing [42], and several interesting applications have been reported in the last years, for example, signal time compression and magnification systems [43], tunable time-delay systems [44], real-time spectrum analyzers [45] and frequency discrimination systems [42], among others. All these systems work satisfactorily at high frequencies and with wide bandwidths.

CDLs with very high time-bandwidth products (defined as the total delay excursion times the operation bandwidth), over ranges of several GHz, can be implemented by using quasiperiodic EBG structures in microstrip technology. To obtain them, the starting point is a single-frequency-tuned EBG structure, with sinusoidal coupling coefficient, of the type proposed in Section 2.4.6. In order to achieve the required group-delay that varies linearly with frequency, the period of the characteristic impedance perturbation is also varied linearly along the propagation axis, z. The characteristic impedance implemented to obtain the CDL in the reported example is [45, 46]:

$$Z_0(z) = Z_{0,\text{ref}} \cdot e^{A \cdot W(z) \cdot \sin\left(\int \zeta(z) \cdot dz\right)} = Z_{0,\text{ref}} \cdot e^{A \cdot W(z) \cdot \sin\left(\frac{2\pi}{l_0} \cdot z + C \cdot z^2 - C \cdot L^2/4\right)} \tag{2.109}$$

where $\zeta(z) = 2\pi/l_0 + 2Cz$ is the spatial angular frequency (that is linearly modulated along z), C is the chirp parameter, and the microstrip line extends from $z = -L/2$ to

$z = L/2$, L being the total device length. The perturbation period of the resulting quasi-periodic EBG structure is

$$l(z) = \frac{2\pi}{\zeta(z)} = \frac{2\pi}{2\pi/l_0 + 2Cz} \tag{2.110}$$

and therefore the frequency locally reflected at position z (calculated through 2.84) is

$$f(z) = \frac{c}{2 \cdot l(z) \cdot \sqrt{\varepsilon_{re}}} = \frac{c}{2 \cdot \sqrt{\varepsilon_{re}}} \cdot \left(\frac{1}{l_0} + \frac{C}{\pi} \cdot z \right) \tag{2.111}$$

where ε_{re} is the effective dielectric constant, c is the speed of light in vacuum, and l_0 is the perturbation period at the center of the device.

As can be seen, the phase-matching condition for resonant Bragg coupling between the forward and backward traveling waves is ideally satisfied at only one position for each frequency. At this position, the propagating wave will be back-reflected. Moreover, since the perturbation is linearly chirped then the mode-coupling location varies linearly with frequency. As a result, the reflection time is also a linear function of frequency. This is equivalent to say that the group delay (in reflection) will vary linearly with frequency, as intended in the CDL. According to (2.111), the CDL implemented following (2.109) will work in reflection with an operation bandwidth:

$$\Delta f = |f(z = L/2) - f(z = -L/2)| = \frac{1}{2\pi} \cdot \frac{c}{\sqrt{\varepsilon_{re}}} \cdot |C| \cdot L \tag{2.112}$$

around a central frequency:

$$f_0 = f(z = 0) = \frac{c}{2 \cdot l_0 \cdot \sqrt{\varepsilon_{re}}} \tag{2.113}$$

and with a group-delay slope, ψ (s/Hz):

$$\psi = \frac{2L\sqrt{\varepsilon_{re}}}{c \cdot \Delta f} = \frac{4\pi \cdot \varepsilon_{re}}{C \cdot c^2} \tag{2.114}$$

The group-delay slope is derived by taking into account that $\Delta f \cdot \psi$ is the time-delay difference between the arrivals at the input of the extreme frequencies of the bandwidth, $f(z = -L/2)$ and $f(z = L/2)$, the former reflected at the input and the latter at the output of the device, respectively (path difference $= 2 \cdot L$).

The three last equations can be inverted to obtain expressions for the main design parameters in (2.109) as a function of the operation bandwidth, Δf (Hz), central frequency, f_0 (Hz), and group-delay slope, ψ (s/Hz):

$$l_0 = \frac{c}{2 \cdot f_0 \cdot \sqrt{\varepsilon_{re}}}$$

$$C = \frac{4\pi \cdot \varepsilon_{re}}{\psi \cdot c^2} \tag{2.115}$$

$$L = \frac{c \cdot |\psi| \cdot \Delta f}{2 \cdot \sqrt{\varepsilon_{re}}}$$

The additional parameters in (2.109) to finish the CDL design are $Z_{0,ref}$, that corresponds to the characteristic impedance of the ports (the integration constant is fixed to $-C \cdot L^2/4$ to ensure input and output ports with $Z_{0,ref}$, assuming that L is a multiple of l_0); A, a nondimensional amplitude factor for the perturbation, and $W(z)$, a windowing function for smoother input and output impedance transitions to avoid partial reflections from the extremes of the structure that give rise to different long-path Fabry–Perot like resonances, which cause undesirable rapid ripple to appear around the mean values in the magnitude and group-delay versus frequency patterns degrading the CDL performance. Furthermore, both negative values of C, which imply upper (higher loss) frequencies to be reflected at the beginning, and asymmetric $W(z)$, which can compensate for the longer lossy round trips, can be used to lead to better equalized reflection losses across the operation band.

To demonstrate the proposed design method, a CDL in microstrip technology is reported. The characteristic impedance of the ports is $Z_{0,ref} = 50\ \Omega$, and the *Rogers RO3010* substrate with dielectric constant $\varepsilon_r = 10.2$, and thickness $h = 1.27$ mm is employed. The central operation frequency is $f_0 = 9$ GHz, and the bandwidth is $\Delta f = 12$ GHz, with a group-delay slope of $\psi = -0.5$ ns/GHz. The design parameters have been calculated using (2.115) to fulfill the response: $l_0 = 6.4$ mm, $L = 50 \cdot l_0$, and $C = -2080\ \text{m}^{-2}$ [45]. A Gaussian asymmetric tapering function is used $W(z) = \exp\left(-4 \cdot ((z - L/4)/L)^2\right)$, and $A = 0.4$. Once all the parameters in (2.109) have been fixed, the impedance variation is implemented as a strip width modulation; see Figure 2.26a. In Figure 2.26b and c, the S_{11} parameter obtained by solving the simplified system of coupled mode equations (2.47a and 2.47b), that is, lossless and single-mode approximation (dotted line), is compared with the simulation employing the commercial software *Agilent Momentum* (thin solid line) and the measurements of the fabricated prototype (thick solid line), showing that the CDL provides the required features of flat magnitude and linear group-delay variation with frequency. The reflection losses are maintained around 3 dB over the entire bandwidth. Finally, the design requirements of central operation frequency, bandwidth and group-delay slope are also properly satisfied.

The main limitation of the CDL structure proposed here is that it operates in reflection, and therefore it requires an additional component to recover the reflected signal. However, this limitation can be avoided by implementing the CDL structure in coupled line technology as explained in Ref. [47].

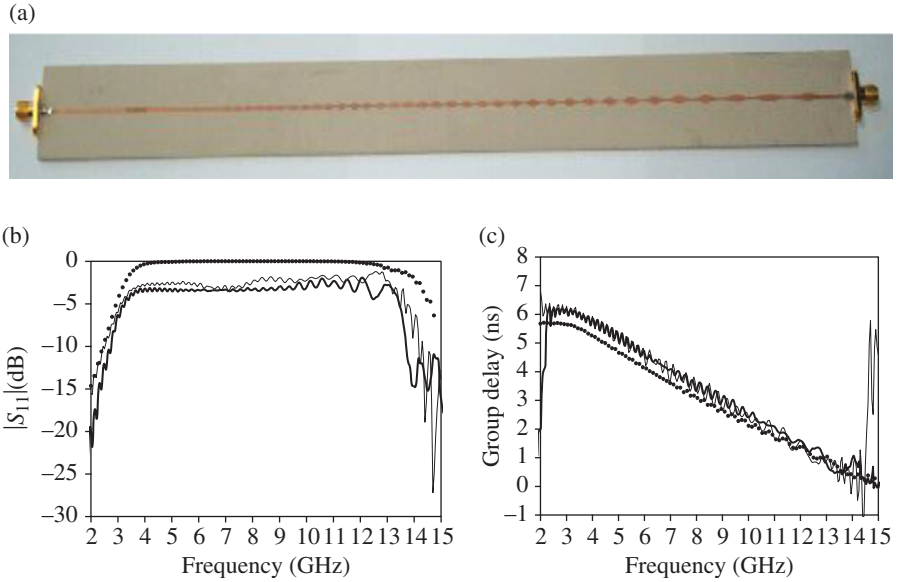

FIGURE 2.26 Photograph of the microstrip CDL (a) and S_{11} parameter of the device: magnitude (b) and group-delay (c) obtained by coupled mode theory (lossless) approximation (dotted line), *Agilent Momentum* (thin solid line) and measurement (thick solid line). Reprinted with permission from Ref. [45], copyright 2003 IEEE.

2.5.2 Applications of Reactively Loaded Lines: The Slow Wave Effect

In the previous applications of EBG-based transmission lines, a periodic perturbation was introduced either in the ground plane or in the conductor strip. However, band gaps in the transmission coefficient of periodic transmission lines can also be achieved by reactively loading the line. Specifically, by periodically loading the line with shunt-connected capacitances, either implemented by lumped elements or with planar semilumped components, significant dispersion arises, pass bands and stop bands appear, and the phase velocity of the lines is reduced. This slow-wave effect is interesting to reduce the size of microwave components. On the other hand, the transmission characteristics of these periodic loaded structures are of interest for the design of planar filters with small size and/or improved performance. All these aspects are discussed in this subsection.

Notice that the coupled mode theory presented in Section 2.4 does not apply to transmission lines periodically loaded with reactive elements. To analyze such artificial lines, the transfer matrix method is a convenient approach. Let us consider a transmission line periodically loaded with shunt-connected capacitances (Fig. 2.27a). The dispersion relation, inferred from (2.22) is:

$$\cos\beta l = \cos kl - \frac{\omega C_{ls} Z_o}{2} \sin kl \tag{2.116}$$

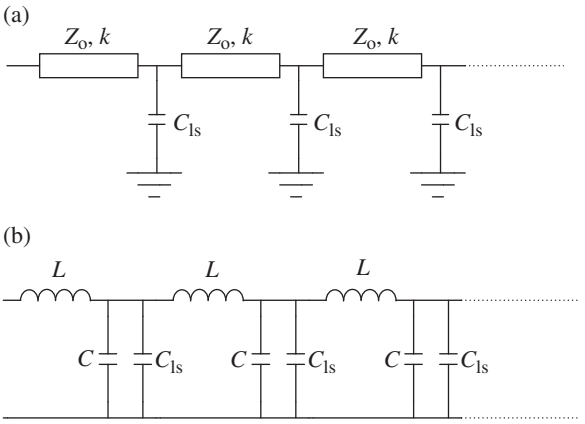

FIGURE 2.27 Transmission line periodically loaded with shunt connected capacitances (a), and lumped-element equivalent circuit model (b).

where k and β are the phase constants of the unloaded and loaded line,[33] respectively, C_{ls} are the loading capacitances, l is the distance between adjacent capacitances (period), and Z_o is the characteristic impedance of the line sections between adjacent capacitances. The dispersion relation is depicted in a Brillouin diagram in Figure 2.28, where $\theta = kl$ is proportional to frequency and $\varphi = \beta l$. This is a representation in a reduced zone, that is, $0 \le \varphi \le \pi$. The structure exhibits a low-pass filter-type response with multiple spurious bands (only the first three bands are visible in the diagram of Fig. 2.28). For design purposes, however, a lumped-element circuit model of the capacitively loaded transmission line is convenient. This circuit model is depicted in Figure 2.27b, where C and L are the per-section capacitance and inductance of the line, respectively. This model is valid under the assumption that $C_{ls} >> C$. According to the lumped-element equivalent circuit of the periodically loaded line, the first pass band of the structure is delimited by the following cutoff frequency

$$f_C = \frac{1}{\pi\sqrt{L(C + C_{ls})}} \tag{2.117}$$

the characteristic (or Bloch) impedance of the loaded line at low frequencies is given by

[33] Notice that in this subsection k is used to designate the phase constant of the unloaded line. Hence, do not confuse with the coupling coefficient parameter (introduced in Section 2.4—see expression 2.66), or with the free-space wavenumber (Section 2.2—see expression 2.10). The use of the same symbol to designate different variables is avoided as much as possible throughout this book. However, exceptions are made either to use the usual symbols for certain variables or to be faithful to the sources/references where the symbols and related expressions are introduced.

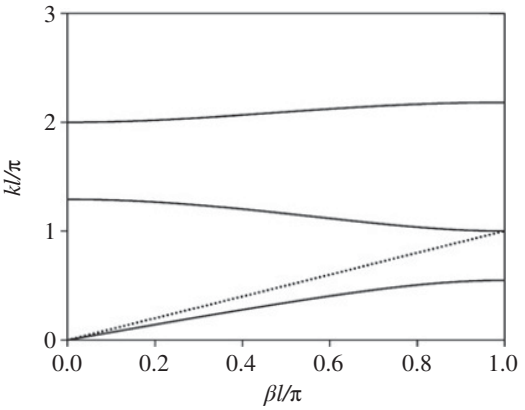

FIGURE 2.28 Typical dispersion diagram of a transmission line periodically loaded with shunt connected capacitances, depicted in a reduced Brillouin zone. The dispersion relation for the unloaded line is also depicted (dotted line). Notice that the smaller slope of the capacitively loaded line at low frequencies (as compared to that of the unloaded line) is indicative of the slow wave effect of capacitively loaded lines.

$$Z_B = \sqrt{\frac{L}{C + C_{ls}}} \tag{2.118}$$

and the lower frequency of the first spurious band is

$$f_S = \frac{1}{2\sqrt{LC}} \tag{2.119}$$

From these equations, the element values can be inferred and the capacitively loaded line can thus be implemented.

The lumped-element equivalent circuit model is only valid in the first band of the structure. Indeed, the circuit model of Figure 2.27b does not exhibit spurious bands. However, the lower frequency of the first spurious band (2.119) can be easily inferred, since $\theta = kl = \pi$ at this frequency. Hence,

$$kl = 2\pi f_S \sqrt{LC} = \pi \tag{2.120}$$

from which (2.119) results.

The cutoff frequency (expression 2.117) can be obtained from (2.116) by considering that $\theta = kl$ is small in the first pass band (which is equivalent to consider that $C_{ls} >> C$). At the cutoff frequency, $\varphi = \beta l = \pi$, and expression (2.116) can be written as

$$-1 = 1 - \frac{(k_c l)^2}{2} - \frac{2\pi f_C C_{ls} Z_o}{2} k_c l \tag{2.121}$$

where the sin and cos functions have been expanded in Taylor series up to the first order, and k_c, given by

$$k_c l = 2\pi f_C \sqrt{LC} \tag{2.122}$$

is the phase constant of the unloaded line at the cutoff frequency. Introducing (2.122) in (2.121), and taking into account that the characteristic impedance of the unloaded line is

$$Z_o = \sqrt{\frac{L}{C}} \tag{2.123}$$

the cutoff frequency can be isolated, and (2.117) is found.

To gain more insight on the validity of the model of Figure 2.27b as C_{ls} increases (as compared to C), the dispersion relations (first band) of three transmission lines loaded with different capacitances have been obtained by means of (2.116), and by applying (2.33) to the unit cell of the circuit of Figure 2.27b. The results, compared in Figure 2.29a, confirm that the dispersion curves inferred from both models are identical in the low-frequency limit, regardless of the value of C_{ls}.[34] This result is expected since at low frequencies the wavelength of the unloaded line is large as compared to the distance, l, between adjacent capacitors. As frequency increases both curves progressively diverge, the difference being a maximum at the cutoff frequency. However, such maximum difference decreases as the difference between C_{ls} and C increases, and the results of Figure 2.29 indicate that for $C_{ls} = 9C$ the relative difference between the cutoff frequencies given by both models is as small as 3.5%. Figure 2.29b compares the Bloch impedance corresponding to the exact (distributed) and approximate (circuit) models for the three considered cases, where it is found that both models tend to give the same values as C_{ls} increases, as expected.

In the next subsections, it is shown that capacitively loaded lines are useful for size reduction (associated to the slow-wave effect) and spurious suppression. Such lines can thus be applied to the design of compact filters with spurious suppression, including lowpass and bandpass filters. The two reported examples are bandpass filters (the application of capacitively loaded lines to lowpass filtering structures can be found in [48–51]).

2.5.2.1 Compact CPW Bandpass Filters with Spurious Suppression By periodically loading a transmission line with shunt capacitances, the phase velocity can be substantially reduced. In the low-frequency limit, the phase velocity of the periodically loaded line, v_{pL}, is given by

[34] Notice that the second and third bands given by the distributed model are also depicted in Figure 2.29a. The presence of these bands is not accounted for by the lumped element model, since it is not valid above the first pass band.

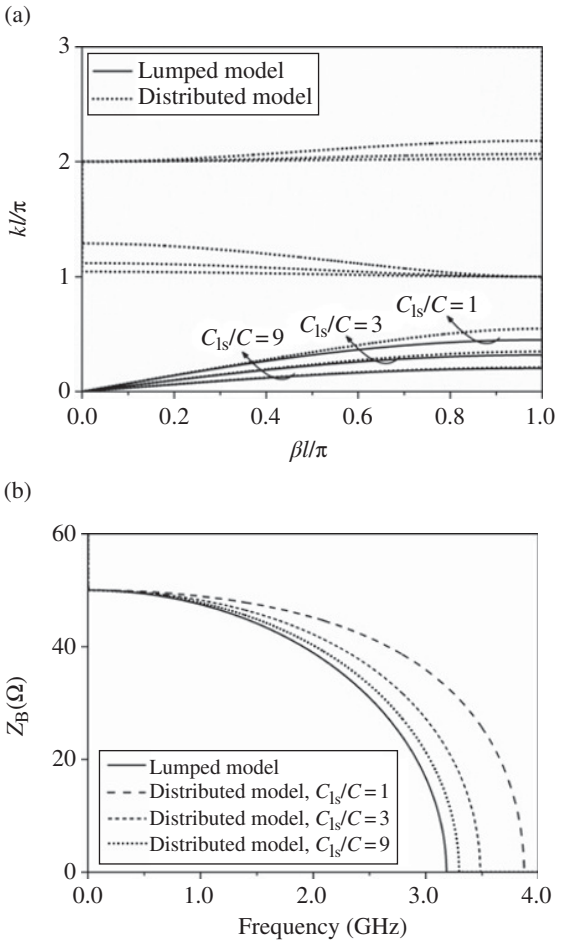

FIGURE 2.29 Dispersion diagram (a) and Bloch impedance (b) of a transmission line periodically loaded with a capacitance C_{ls} of the indicated value. The curves corresponding to the distributed and lumped-element circuit models are indicated in dashed and solid lines, respectively. For the three cases, $L = 5$ nH and $C + C_{ls} = 2$ pF, so that the Bloch impedance at low frequencies and the cutoff frequency (lumped-element model) are identical for the three considered cases. Notice that the values of kl at the cutoff frequency are different since they depend on C (see expression 2.122), which is different for the three considered cases.

$$v_{pL} = \frac{l}{\sqrt{L(C + C_{ls})}} \tag{2.124}$$

The effect of such phase velocity reduction is a decrease of the guided wavelength; hence, significant size reduction of distributed circuits implemented with such periodically loaded lines can be achieved. Such artificial lines, also referred to as

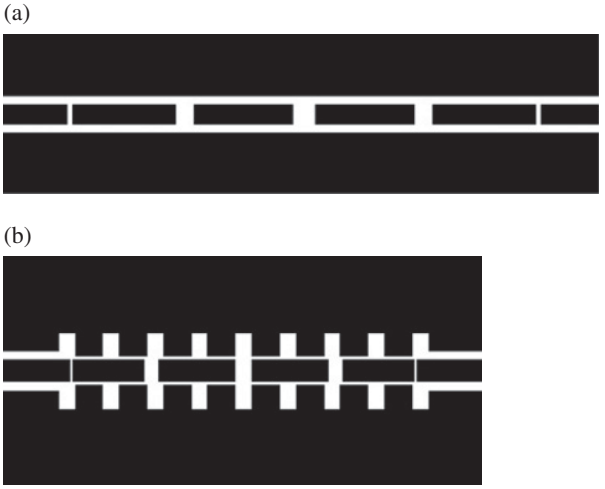

FIGURE 2.30 Layouts of the conventional (a) and periodic-loaded (b) CPW bandpass filters. The layouts are drawn to scale, the length of the conventional filter being 5.6 cm. Reprinted with permission from Ref. [54], copyright 2004 John Wiley & Sons.

slow-wave transmission lines, or simply slow-wave structures, are an alternative to high dielectric constant substrates for device miniaturization. Moreover, since these capacitively loaded lines exhibit stop bands, they can be used to simultaneously reduce the size of distributed circuits and suppress undesired bands (as pointed out before).

In CPW technology, the loading capacitances can be implemented by means of T-shaped planar structures, as reported in Refs [50, 51]. The slow-wave effect can also be achieved by periodically approaching the conductor strip and ground planes. This idea was applied by Görur *et al*. [52, 53] to the design of compact resonators in CPW technology and by Martín *et al*. [54] to the design of compact capacitively (gap) coupled resonator bandpass filters (see the example provided in Section 1.6.4, corresponding to a conventional implementation). The details of the design of these filters can be found in Ref. [54]. Essentially, the periodic perturbation (providing capacitive loading) has been determined to obtain a cutoff frequency beyond the pass band of interest, but below the first harmonic band. In this way, spurious elimination is achieved. Moreover, the line perturbation effectively increases the capacitance of the line, decreases the phase velocity (slow-wave effect), and hence reduces the length of the different resonators forming the filter.[35] The filter described in Ref. [54] is a fourth-order bandpass filter with central frequency $f_o = 6$ GHz and 10% fractional bandwidth. It is depicted in Figure 2.30 and compared with the conventional

[35] A detailed design process of the capacitively loaded slow wave transmission lines using expressions (2.117)–(2.119) is given in reference to the bandpass filter of the next subsection, also based on slow-wave transmission-line sections, but implemented in microstrip technology.

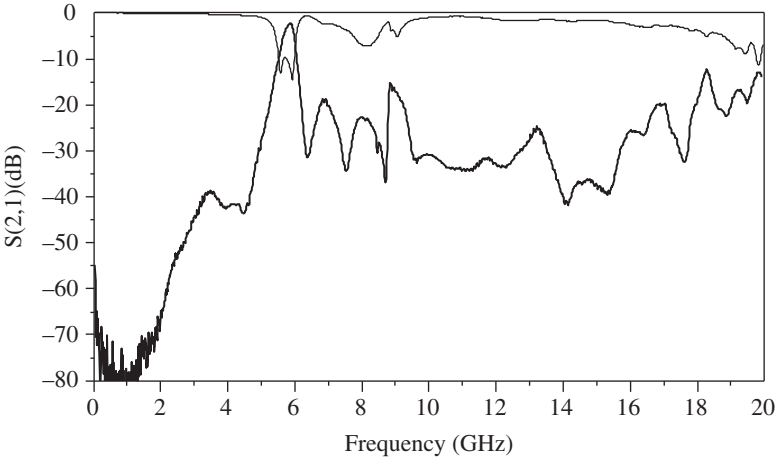

FIGURE 2.31 Measured insertion (bold line) and return (thin line) loss for the periodic-loaded filter of Figure 2.30b. Reprinted with permission from Ref. [54], copyright 2004 John Wiley & Sons.

implementation (designed on the same substrate—*Rogers RO3010* with $\varepsilon_r = 10.2$, $h =$ 1.27 mm—with identical central frequency). Roughly 30% size reduction is achieved by means of the slow-wave periodic structure. The measured frequency response of the device is depicted in Figure 2.31. The device is spurious free in a wide band due to the effects of periodicity. This concept has been applied to the miniaturization of other components, such as hybrids and couplers [55].

Other periodic slow wave structures based on inductive loading [56], or combined inductive and capacitive loading [57–62] have also been reported. The topic of slow-wave transmission lines has attracted much attention in recent years for their potential in size reduction of distributed circuits, and other different approaches (out of the scope of this book) have been reported [63], including slow-wave transmission lines for passive and active CMOS devices operating at millimetre wavelengths [64–69].

2.5.2.2 Compact Microstrip Wideband Bandpass Filters with Ultrawideband Spurious Suppression Capacitively loaded lines can also be implemented in microstrip technology by means of patch capacitances. These structures can also be applied to the design of compact bandpass filters (due to the inherent slow-wave effect). However, since high capacitance values can be achieved by means of capacitive patches, the most relevant aspect of these periodic loaded microstrip lines is the huge achievable stop bands, which are very interesting to suppress spurious bands over a very wide frequency range. As an illustrative example of capacitively loaded microstrip lines, a wideband bandpass filter is considered, where some of the transmission line sections are substituted by patch loaded lines [70]. The filter consists of a cascade of shunt stubs of equal length, alternating with

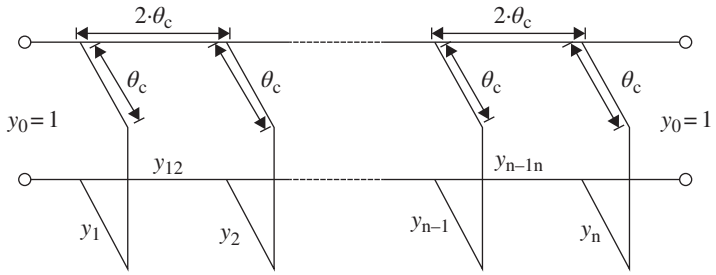

FIGURE 2.32 Schematic of the wideband bandpass filter where y_i and y_{jk} are the normalized characteristic admittances of the stubs and transmission lines, respectively.

transmission lines with twice the stub electrical length. The analysis of this type of filters was done by Levy [71]. A very interesting characteristic of these filters is that by using n stubs, an insertion function of degree $2n-1$ is implemented. These filters are useful to generate wide transmission bands, although wideband spurious are also present in their frequency response. The schematic of the filter is depicted in Figure 2.32. The network shown in Figure 2.32 implements the transfer function described in expression (2.125a) as a function of the normalized frequency variable $\theta = \theta_c f/f_c$ [72]:

$$|S_{21}(\theta)|^2 = \frac{1}{1+\kappa^2 F_n^2(\theta)} \tag{2.125a}$$

with

$$F_n(\theta) = \frac{\left(1+\sqrt{1-x_c^2}\right)\cdot T_{2n-1}\left(\frac{x}{x_c}\right) - \left(1-\sqrt{1-x_c^2}\right)\cdot T_{2n-3}\left(\frac{x}{x_c}\right)}{2\cdot\cos\left(\frac{\pi}{2}-\theta\right)} \tag{2.125b}$$

$$x = \sin\left(\frac{\pi}{2}-\theta\right) \tag{2.125c}$$

$$x_c = \sin\left(\frac{\pi}{2}-\theta_c\right) \tag{2.125d}$$

where $T_n = \cos(n\cdot\cos^{-1}(x))$ and κ is the pass band ripple constant. The bandwidth of the filter is delimited by the frequencies f_c and $(\pi/\theta_c - 1)f_c$; therefore, the bandwidth can be controlled by the value of the angle θ_c.

As an illustrative example, a $n=3$ prototype with $f_c = 1.4$ GHz and $\theta_c = 35°$ (that implies a 4.8 GHz bandwidth) is implemented. To determine the impedance values of the short-circuit stubs and line elements, the tabulated element values supplied by Hong and Lancaster in their text book [72] for optimum distributed highpass

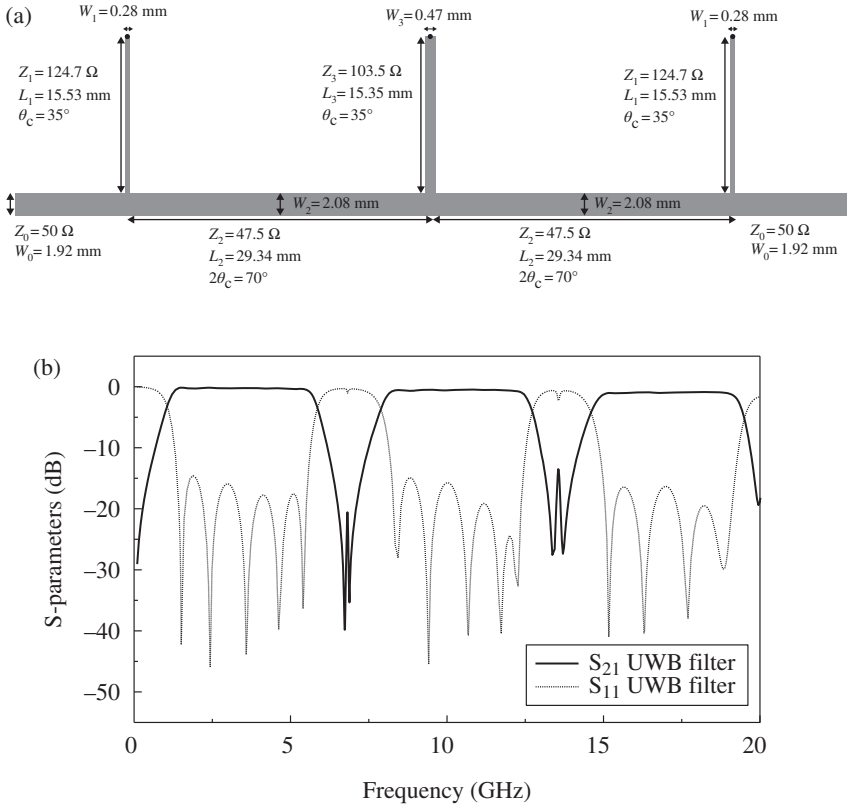

FIGURE 2.33 (a) Layout of the wideband bandpass filter including electrical parameters and geometry of transmission lines and stubs. (b) EM simulation of the frequency response of the filter. Reprinted with permission from Ref. [70], copyright 2006 IEEE.

filters are used. The resulting impedance values are shown in Figure 2.33. The simulation results depicted in Figure 2.33b correspond to the structure described in Figure 2.33a, implemented in an *Arlon* substrate with dielectric constant $\varepsilon_r = 2.4$ and thickness $h = 0.675$ mm. Five reflection zeros can be observed in the transmission bands, such as one expects on account of the $2n - 1$ degree of the filter function ($n = 3$ in our case). The structure of Figure 2.33 is the conventional implementation.

The capacitively loaded structure is obtained by replacing the interstub transmission line sections with patch-loaded lines (with two unit cells). The electrical length of these lines is 70°, whereas the characteristic impedance is 47.5 Ω. The phase shift per cell is given by

$$\phi = 2\pi \cdot f \sqrt{L(C + C_{ls})} \tag{2.126}$$

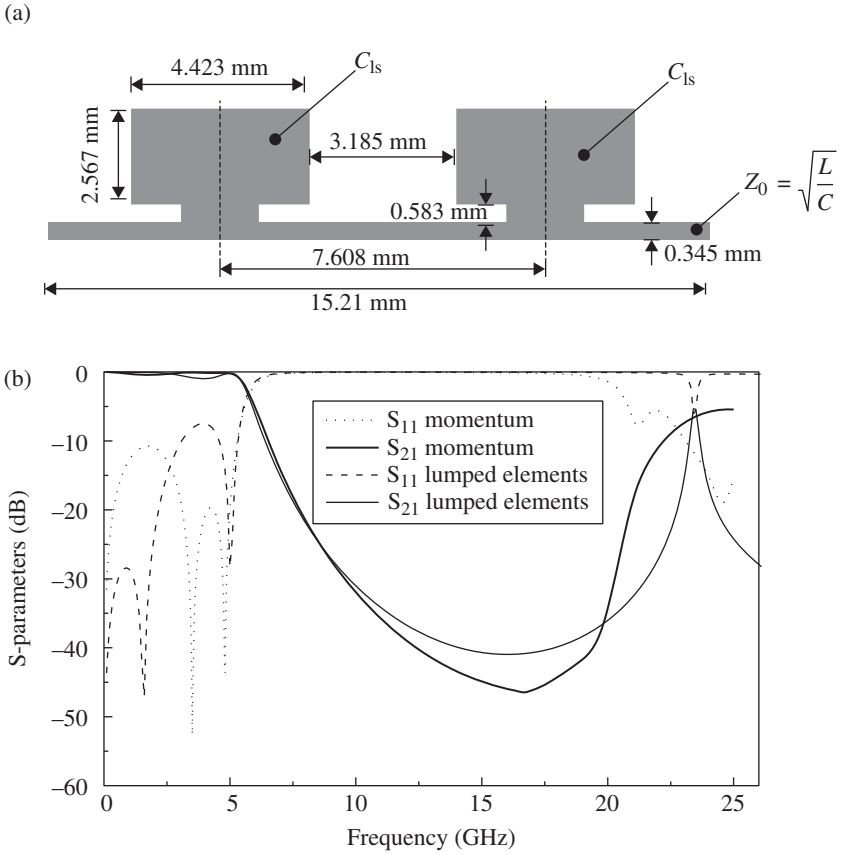

FIGURE 2.34 (a) Layout of the periodic-loaded structure in microstrip technology and (b) electrical and EM simulation. Reprinted with permission from Ref. [70], copyright 2006 IEEE.

By forcing (2.118) and (2.126) to obtain the required electrical characteristics (i.e., $\phi = 35^\circ$ at 1.4 GHz and $Z_B = 47.5\,\Omega$) and by setting f_s (expression 2.119) to $f_s =$ 22 GHz in order to obtain a huge rejection band, the electrical parameters of the patch (capacitively) loaded line can be inferred. The results are as follows: $C = 0.17$ pF, $L = 3.1$ nH and $C_{ls} = 1.2$ pF. With these values, the impedance of the unloaded line is $Z_o = 123.5\,\Omega$, and the cutoff frequency of the periodic-loaded line is $f_C =$ 5.6 GHz, that is, it lies between the pass band of interest and the first spurious frequency of the conventional filter.

The layout of the patch-loaded transmission line sections was obtained by means of an optimization procedure by using *Agilent Momentum*. It is depicted in Figure 2.34 together with the simulated frequency response. The band gap extends up to more than 20 GHz (as required). Hence, it is expected that by introducing such lines in the filter layout, the frequency response is free of spurious up to very high frequencies.

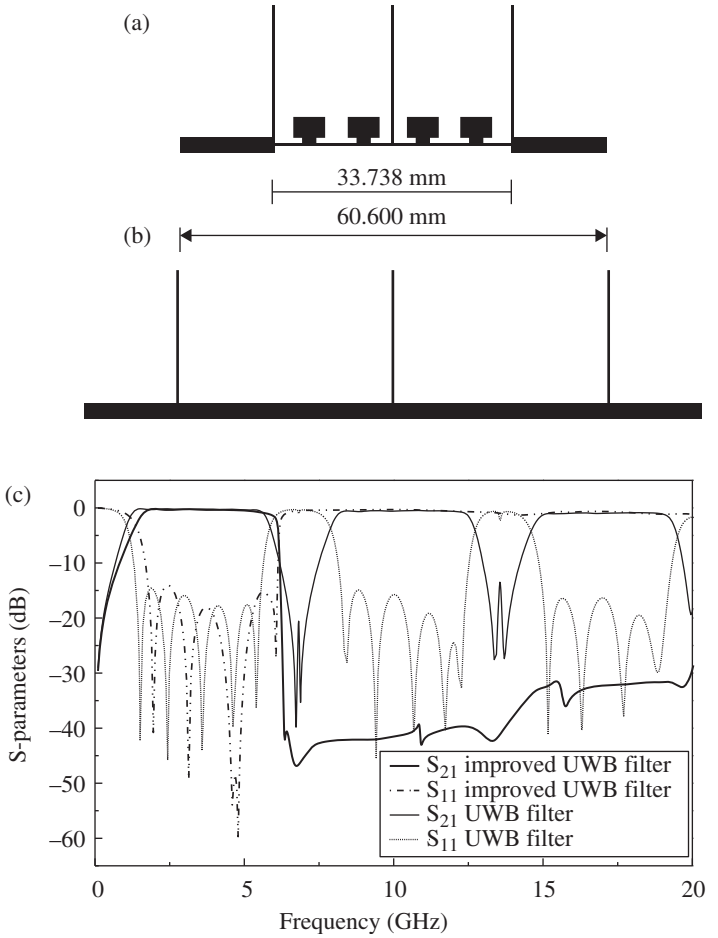

FIGURE 2.35 Layout of the patch-loaded filter (a) standard filter (b) and EM simulation of both filters (c). The filters are designed and implemented using an *Arlon* substrate with $\varepsilon_r = 2.4$ and thickness $h = 0.675$ mm. Reprinted with permission from Ref. [70], copyright 2006 IEEE.

A comparative layout of the conventional and capacitively loaded (patch-loaded) filters and the corresponding simulated frequency responses are depicted in Figure 2.35. The photograph of the fabricated patch-loaded filter is shown in Figure 2.36, jointly with the measured frequency response. The out-of-band performance is good, with a rejection level better than −30 dB up to 20 GHz. In-band losses are lower than 0.9 dB and return losses are better than 10 dB. Finally, approximately 50% length reduction is obtained by using the capacitively loaded filter.

A balanced (differential) version of this type of filters, covering the frequency spectrum assigned for ultrawideband (UWB) communications (3.1–10.6 GHz), is reported in Ref. [73].

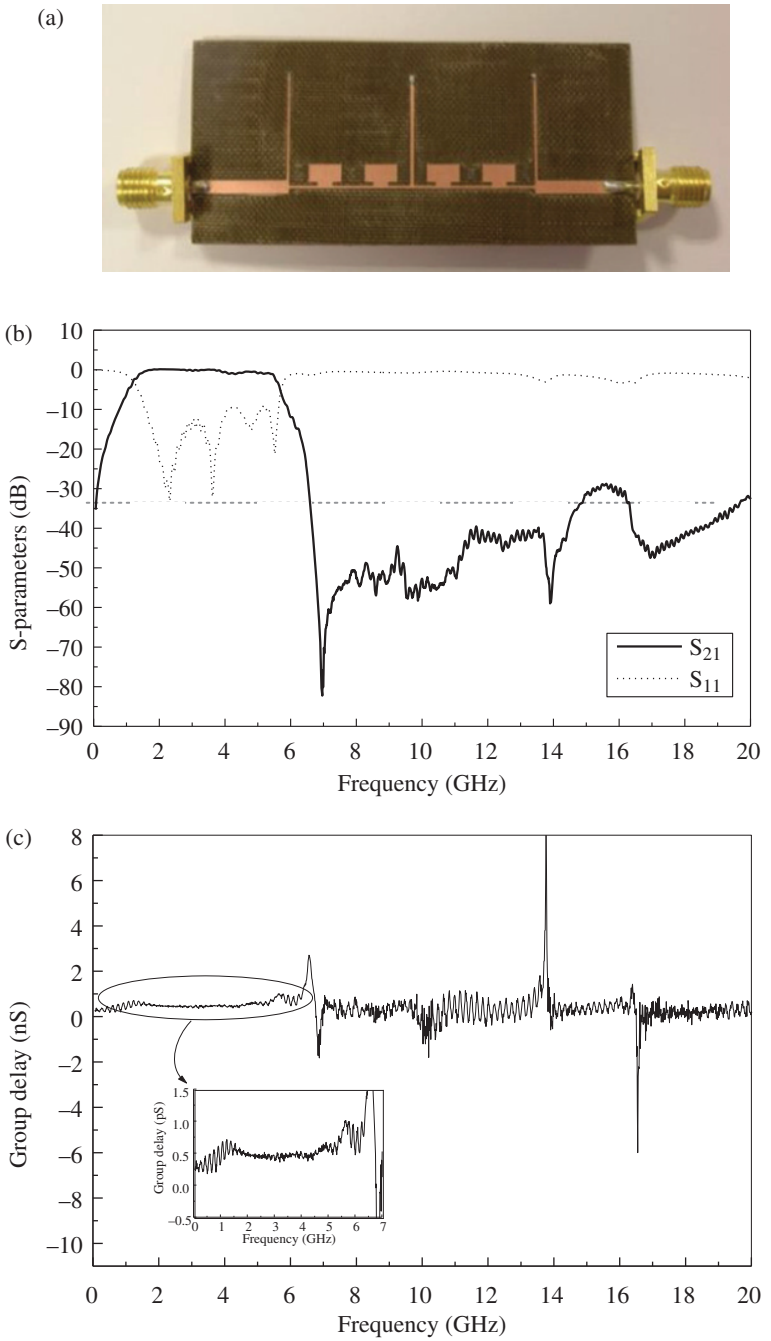

FIGURE 2.36 (a) Picture of the fabricated patch-loaded filter, (b) measured S-parameters, and (c) measured group delay. Reprinted with permission from Ref. [70], copyright 2006 IEEE.

To end this chapter, let us mention that although the most intensive research activity on periodic transmission lines (EBG-based and reactively loaded lines) was carried out in the late nineties and first years of this century, there is still activity on this topic. In particular, EBGs have been combined with coupled lines for the design of coupled line directional couplers with enhanced coupling factor [22, 74, 75]. By properly modulating the common-mode and differential-mode characteristic impedances, it is possible to achieve contra-phase reflection coefficients for the even and odd modes and, consequently, redirect the reflected signal to the coupled port. Another recent application concerns the design of differential lines with common-mode suppression [76]. In this case, the common-mode impedance is periodically modulated, whereas the differential-mode impedance is kept uniform along the line. The result is a band gap for the common-mode, whereas the line is transparent for the differential signals (other techniques for common-mode suppression in differential lines are pointed out in Chapter 6).

REFERENCES

1. L. Brillouin, *Wave Propagation in Periodic Structures: Electric Filters and Crystal Lattices*, 2nd Edition, Dover Publications, New York, 1953.
2. A. A. Oliner, "Radiating periodic structures: analysis in terms of k vs. β diagrams," in *Short Course on Microwave Field and Network Techniques*, Polytechnic Institute of Brooklyn, New York, 1963.
3. A. Yariv and P. Yeh, *Optical Waves in Crystals*, Wiley, New York, 1984.
4. R. E. Collin, *Foundations for Microwave Engineering*, 2nd Edition, McGraw Hill, Singapore, 1992.
5. J. D. Joannopoulos, R. D. Meade, and J. N. Winn, *Photonic Crystals: Molding the Flow of Light*, Princeton University Press, Princeton, NJ, 1995.
6. A. A. Oliner, "Leaky-wave antennas," in *Antenna Engineering Handbook*, R. C. Johnson, Ed. McGraw-Hill, New York, 1993.
7. F. B. Gross, Ed. *Frontiers in Antennas: Next Generation Design & Engineering*, Mc Graw Hill, New York, 2011.
8. J. L. Volakis, Ed. *Antenna Engineering Handbook*, 4th Edition, Mc Graw Hill, New York, 2007.
9. C. A. Balanis, Ed. *Modern Antenna Handbook*, Wiley, Hoboken, NJ, 2008.
10. D. M. Pozar, *Microwave Engineering*, 2nd Ed., Addison-Wesley, Reading, MA, 1998.
11. F. Sporleder and H. G. Unger, *Waveguide Tapers, Transitions and Couplers,* Peter Peregrinus, London, UK, 1979.
12. V. V. Shevchenko, *Continuos Transitions in Open Waveguides,* Golem, Boulder, CO, 1971.
13. B. Z. Katsenelenbaum, L. Mercader, M. Pereyaslavets, M. Sorolla, and M. Thumm, *Theory of Nonuniform Waveguides—the Cross-Section Method*, IEE Electromagnetic Waves Series, 44, The Institution of Engineering and Technology, London, UK, 1998.

14. T. Lopetegi, *Photonic band gap structures in microstrip technology: study using the coupled mode formalism and applications*, PhD Thesis Dissertation, Universidad Pública de Navarra, Pamplona, Spain, 2002.
15. D. Marcuse, *Theory of Dielectric Optical Waveguides*, 2nd Ed., Academic Press, San Diego, CA, 1991.
16. T. Lopetegi, M. A. G. Laso, M. J. Erro, M. Sorolla, and M. Thumm, "Analysis and design of periodic structures for microstrip lines by using the coupled mode theory," *IEEE Microw. Wireless Compon. Lett.*, vol. **12**, pp. 441–443, 2002.
17. I. Bahl and P. Barthia, *Microwave Solid State Circuit Design*, 2nd Edition., Wiley, New York, 2003.
18. V. Radisic, Y. Qian, R. Coccioli, and T. Itoh, "Novel 2-D photonic bandgap structure for microstrip lines," *IEEE Microw. Guided Wave Lett.*, vol. **8**, pp. 69–71, 1998.
19. F. Falcone, T. Lopetegi, and M. Sorolla, "1-D and 2-D photonic bandgap microstrip structures," *Microw. Opt. Technol. Lett.*, vol. **22**, pp. 411–412, 1999.
20. H. Kogelnik and C. V. Shank, "Coupled-wave theory of distributed feedback lasers," *J. Appl. Phys.*, vol. **43**, pp. 2327–2335, 1972.
21. A. Yariv and M. Nakamura, "Periodic structures for integrated optics," *IEEE J. Quantum Electron.*, vol. **13**, pp. 233–253, 1977.
22. I. Arnedo, M. Chudzik, J. Schwartz, I. Arregui, A. Lujambio, F. Teberio, D. Benito, M. A. G. Laso, D. Plant, J. Azaña, and T. Lopetegi, "Analytical solution for the design of planar EBG structures with spurious-free frequency response," *Microw. Opt. Technol. Lett.*, vol. **54**, pp. 956–960, 2012.
23. E. F. Bolinder, "Fourier transforms in the theory of inhomogeneous transmission lines," *Proc. IRE*, vol. **38**, pp. 1354, 1950.
24. E. Yablonovitch, "Photonic band gap structures," *J. Opt. Soc. Am. B* **10**, pp. 283–295, 1993.
25. Y. Qian, V. Radistic, and T. Itoh, "Simulation and experiment of photonic band-gap structures for microstrip circuits," *Proc. Asia-Pacific Microw. Conf.*, Hong Kong, December 1997, pp. 585–588.
26. T. J. Ellis and G. M. Rebeiz, "MM-w ave tapered slot antennas on micromachined photonic bandgap dielectrics," *IEEE MTT-S Int. Microw. Symp. Dig*., San Francisco, CA, June 1996, pp. 1157–1160.
27. M. J. Erro, M. A. G. Laso, T. Lopetegi, D. Benito, M. J. Garde, and M. Sorolla, "Optimization of tapered bragg reflectors in microstrip technology," *Int. J. Infrared Milli. Waves*, vol. **21**, pp. 231–245, 2000.
28. K. O. Hill and G. Meltz, "Fiber Bragg grating technology fundamentals and overview," *J. Lightwave Technol.*, vol. **15**, pp. 1263–1276, 1997.
29. M. A. G. Laso, T. Lopetegi, M. J. Erro, D. Benito, M. J. Garde, and M. Sorolla, "Novel wideband photonic bandgap microstrip structures," *Microw. Opt. Technol. Lett.*, vol. **24**, pp. 357–360, 2000.
30. F. Falcone, T. Lopetegi, M. Irisarri, M. A. G. Laso, M. J. Erro, and M. Sorolla, "Compact photonic bandgap microstrip structures," *Microw. Opt. Technol. Lett.*, vol. **23**, pp. 233–236, 1999.
31. M. A. G. Laso, T. Lopetegi, M. J. Erro, D. Benito, M. J. Garde, and M. Sorolla, "Multiple-frequency-tuned photonic bandgap microstrip structures," *IEEE Microw. Guided Wave Lett.*, vol. **10**, pp. 220–222, 2000.

32. T. Lopetegi, F. Falcone, and M. Sorolla, "Bragg reflectors and resonators in microstrip technology based on electromagnetic crystal structures," *Int. J. Infrared Milli. Waves*, vol. **20**, pp. 1091–1102, 1999.

33. V. L. Bratman, G. G. Denisov, N. S. Ginzburg, and M. I. Petelin, "FEL's with Bragg reflection resonators: cyclotron autoresonance masers versus ubitrons," *IEEE J. Quantum Electron.*, vol. **19**, pp. 282–296, 1983.

34. T.-Y. Yun and K. Chang, "Uniplanar one-dimensional photonic-bandgap structures and resonators," *IEEE Trans. Microw. Theory Techn.*, vol. **49**, pp. 549–553, 2001.

35. T. Lopetegi, M. A. G. Laso, J. Hernández, M. Bacaicoa, D. Benito, M. J. Garde, M. Sorolla, and M. Guglielmi, "New microstrip wiggly-line filters with spurious passband suppression," *IEEE Trans. Microw. Theory Techn.*, vol. **49**, pp 1593–1598, 2001.

36. T. Lopetegi, M. A. G. Laso, F. Falcone, F. Martín, J. Bonache, L. Pérez-Cuevas, and M. Sorolla, "Microstrip wiggly line band pass filters with multispurious rejection," *IEEE Microw. Wireless Compon. Lett.*, vol. **14**, pp.531–533, 2004.

37. V. Radisic, Y. Qian, and T. Itoh, "Broad-band power amplifier using dielectric photonic bandgap structure," *IEEE Microw. Guided Wave Lett.*, vol. **8**, pp. 13–14, 1998.

38. C. Y. Hang, V. Radisic, Y. Qian, and T. Itoh, "High efficiency power amplifier with novel PBG ground plane for harmonic tuning," *IEEE MTT-S Int. Microw. Symp. Dig.*, Anaheim, CA, June 1999, pp. 807–810.

39. F. R. Yang, Y. Qian, and T. Itoh, "A novel uniplanar compact PBG structure for filter and mixer applications," *IEEE MTT-S Int. Microw. Symp. Dig.*, Anaheim, CA, June 1999, pp. 919–922.

40. Q. Xue, K. M. Shum, and C. H. Chan, "Novel oscillator incorporating a compact microstrip resonant cell," *IEEE Microw. Wireless Compon. Lett.*, vol. **11**, pp. 202–204, 2001.

41. Y. T. Lee, J. S. Lim, J. S. Park, D. Ahn, and S. Nam, "A novel phase noise reduction technique in oscillators using defected ground structure," *IEEE Microw. Wireless Compon. Lett.*, vol. **12**, pp. 39–41, 2002.

42. C. Caloz, S. Gupta, Q. Zhang, and B. Nikfal, "Analog signal processing: a possible alternative or complement to dominantly digital radio schemes," *Microw. Mag.*, vol. **14**, pp. 87–103, 2013.

43. J. D. Schwartz, J. Azaña, and D. V. Plant, "A fully electronic system for the time magnification of ultra-wideband signals," *IEEE Trans. Microw. Theory Techn.*, vol. **55**, pp. 327–334, 2007.

44. J. D. Schwartz, I. Arnedo, M. A. G. Laso, T. Lopetegi, J. Azaña, and D. V. Plant, "An electronic UWB continuously tunable time-delay system with nanosecond delays," *IEEE Microw. Wireless Compon. Lett.*, vol. **18**, pp. 103–105, 2008.

45. M. A. G. Laso, T. Lopetegi, M. J. Erro, D. Benito, M. J. Garde, M. A. Muriel, M. Sorolla, and M. Guglielmi, "Real-time spectrum analysis in microstrip technology," *IEEE Trans. Microw. Theory Techn.*, vol. **51**, pp. 705–717, 2003.

46. M. A. G. Laso, T. Lopetegi, M. J. Erro, D. Benito, M. J. Garde, M. A. Muriel, M. Sorolla, and M. Guglielmi, "Chirped delay lines in microstrip technology," *IEEE Microw. Wireless Compon. Lett.*, vol. **11**, pp. 486–488, 2001.

47. A. Lujambio, I. Arnedo, M. Chudzik, I. Arregui, T. Lopetegi, and M. A. G. Laso, "Dispersive delay line with effective transmission-type operation in coupled-line technology," *IEEE Microw. Wireless Compon. Lett.*, vol. **21**, pp. 459–461, 2011.

48. F. Martín, F. Falcone, J. Bonache, T. Lopetegi, M. A. G. Laso, and M. Sorolla, "New periodic-loaded electromagnetic bandgap coplanar waveguide with complete spurious passband suppression," *IEEE Microw. Wireless Compon. Lett.*, vol. **12**, pp. 435–437, 2002.
49. F. Martín, F. Falcone, J. Bonache, T. Lopetegi, M. A. G. Laso, and M. Sorolla, "Analysis of the reflection properties in electromagnetic bandgap coplanar waveguides loaded with reactive elements," *Prog. Electromag. Res.,* vol. **42**, pp. 27–48, 2003.
50. F. Martín, F. Falcone, J. Bonache, M. A. G. Laso, T. Lopetegi, and M. Sorolla, "New CPW low pass filter based on a slow wave structure," *Microw. Opt. Technol. Lett.*, vol. **38**, pp. 190–193, 2003.
51. F. Martín, F. Falcone, J. Bonache, M. A. G. Laso, T. Lopetegi, and M. Sorolla, "Dual electromagnetic bandgap CPW structures for filter applications," *IEEE Microw. Wireless Compon. Lett.*, vol. **13**, pp. 393–395, 2003.
52. A. Görür, "A novel coplanar slow-wave structure," *IEEE Microw. Guided Wave Lett.*, vol. **4**, pp. 86–88, 1994.
53. A. Görür, C. Karpuz, and M. Alkan, "Characteristics of periodically loaded CPW structures," *IEEE Microw. Guided Wave Lett.*, vol. **8**, pp. 278–280, 1998.
54. F. Martín, J. Bonache, I. Gil, F. Falcone, T. Lopetegi, M. A. G. Laso, and M. Sorolla, "Compact spurious free CPW band pass filters based on electromagnetic bandgap structures," *Microw. Opt. Technol. Lett*, vol. **40**, pp. 146–148, 2004.
55. K. W. Eccleston and S. H. M. Ong, "Compact planar microstripline branch-line and rat-race couplers," *IEEE Trans. Microw. Theory Techn.,* vol. **51**, pp 2119–2125, 2003.
56. L. Zhu, "Guided-wave characteristics of periodic microstrip lines with inductive loading: slow-wave and bandstop behaviors," *Microw. Opt. Technol. Lett.*, vol. **41**, pp. 77–79, 2004.
57. F.-R. Yang, K.-P. Ma, Y. Qian, and T. Itoh, "A uniplanar compact photonic-bandgap (UC-PBG) structure and its applications for microwave circuits," *IEEE Trans. Microw. Theory Techn.*, vol. **47**, pp. 1509–1514, 1999.
58. J. Sor, Y. Qian, and T. Itoh, "Miniature low-loss CPW periodic structures for filter applications," *IEEE Trans. Microw. Theory Techn.*, vol. **49**, pp. 2336–2341, 2001.
59. D. Nesic, "A new type of slow-wave 1-D PBG microstrip structure without etching in the ground plane for filter and other applications," *Microw. Opt. Technol. Lett.*, vol. **33**, pp. 440–443, 2002.
60. S.-G. Mao, M.-Y. Chen, "A novel periodic electromagnetic bandgap structure for finite-width conductor-backed coplanar waveguides," *IEEE Microw. Wireless Compon. Lett.*, vol. **11**, pp. 261–263, 2001.
61. S.-G. Mao, C.-M. Chen, and D.-C. Chang, "Modeling of slow-wave EBG structure for printed-bowtie antenna array," *IEEE Antennas Wireless Propag. Lett.*, vol. **1**, pp. 124–127, 2002.
62. C. Zhou and H. Y. David Yang, "Design considerations of miniaturized least dispersive periodic slow-wave structures," *IEEE Trans. Microw. Theory Techn.*, vol. **56**, pp. 467–474, 2008.
63. J. Wang, B.-Z. Wang, Y.-X. Guo, L. C. Ong, and S. Xiao "A compact slow-wave microstrip branch-line coupler with high performance," *IEEE Microw. Wireless Compon. Lett.*, vol. **17**, pp. 501–503, 2007.

64. N. Yang, C. Caloz, and K. Wu, "Slow-wave rail coplanar strip (RCPS) line with low impedance capability," *Proc. 29th URSI General Assembly*, Chicago, IL, August 2008.

65. D. Kaddour, H. Issa, A.-L. Franc, N. Corrao, E. Pistono, F. Podevin, J.-M. Fournier, J.-M. Duchamp, and P. Ferrari, "High-Q slow-wave coplanar transmission lines on 0.35-μm CMOS process," *IEEE Microw. Wireless Compon. Lett.*, vol. **19**, pp. 542–544, 2009.

66. T. LaRocca, J. Y.-C. Liu, and M.-C. F. Chang, "60 GHz CMOS amplifiers using transformer-coupling and artificial dielectric differential transmission lines for compact design," *IEEE J. Solid State Circ.*, vol. **44**, pp. 1425–1435, 2009.

67. J. J. Lee and C. S. Park, "A slow-wave microstrip line with a high-Q and a high dielectric constant for millimeter-wave CMOS applications," *IEEE Microw. Wireless Compon. Lett.*, vol. **20**, pp. 381–383, 2010.

68. A.-L. Franc, D. Kaddour, H. Issa, E. Pistono, N. Corrao, J.-M. Fournier, and P. Ferrari, "Impact of technology dispersion on slow-wave high performance shielded CPW transmission lines characteristics," *Microw. Opt. Technol. Lett.*, vol. **52**, pp. 2786, 2789, 2010.

69. M. Abdel Aziz, H. Issa, D. Kaddour, F. Podevin, A. M. E. Safwat, E. Pistono, J.-M. Duchamp, A. Vilcot, J.-M. Fournier, and P. Ferrari, "Slow-wave high-Q coplanar striplines in CMOS technology and their RLCG model," *Microw. Opt. Technol. Lett.*, vol. **54**, pp. 650–654, 2012.

70. J. García-García J. Bonache, and F. Martín, "Application of electromagnetic bandgaps (EBGs) to the design of ultra wide band pass filters (UWBPFs) with good out-of-band performance," *IEEE Trans. Microw. Theory Techn.*, vol. **54**, pp. 4136–4140, 2006.

71. R. Levy, "A new class of distributed prototype filters with applications to mixed lumped/distributed component design," *IEEE Trans. Microw. Theory Techn.*, vol. **18**, pp. 1064–1071, 1970.

72. J.-S. Hong and M. L. Lancaster, *Microstrip Filters for RF/Microwave Applications*, Wiley, Hoboken, NJ, 2001.

73. P. Vélez, J. Bonache, J. Mata-Contreras, and F. Martín, "Ultra-wideband (UWB) balanced bandpass filters with wide stop band and intrinsic common-mode rejection based on embedded capacitive electromagnetic bandgaps (EBG)," *IEEE MTT-S Int. Microwave Symp. Dig.*, Tampa, FL, June 2014.

74. M. Chudzik, I. Arnedo, A. Lujambio, I. Arregui, F. Teberio, M. A. G. Laso, and T. Lopetegi, "Microstrip coupled-line directional coupler with enhanced coupling based on EBG concept," *Electron. Lett.*, vol. **47**, pp. 1284–1286, 2011.

75. M. Chudzik, I. Arnedo, A. Lujambio, I. Arregui, F. Teberio, D. Benito, T. Lopetegi, and M. A. G. Laso, "Design of EBG microstrip directional coupler with high directivity and coupling," *Proc. 42th Eur. Microw. Conf.*, Amsterdam, the Netherlands, October 2012.

76. P. Vélez, J. Bonache, and F. Martín, "Differential microstrip lines with common-mode suppression based on electromagnetic bandgaps (EBGs)," *IEEE Antennas Wireless Propag. Lett.*, vol. **14**, pp. 40–43, 2015.